HHS Public Access

Author manuscript

Neuron. Author manuscript; available in PMC 2023 May 04.

Published in final edited form as:

Neuron. 2022 May 04; 110(9): 1498–1515.e8. doi:10.1016/j.neuron.2022.01.026.

Rebuilding essential active zone functions within a synapse

Chao Tan[1], **Shan Shan H. Wang**[1], **Giovanni de Nola**[1], **Pascal S. Kaeser**[1,*]

[1]Department of Neurobiology, Harvard Medical School, Boston, MA 02115

Summary

Presynaptic active zones are molecular machines that control neurotransmitter secretion. They form sites for vesicle docking and priming, and couple vesicles to Ca^{2+} entry for release-triggering. The complexity of active zone machinery has made it challenging to determine its mechanisms in release. Simultaneous knockout of the active zone proteins RIM and ELKS disrupts active zone assembly, abolishes vesicle docking, and impairs release. We here rebuild docking, priming and Ca^{2+}-secretion coupling in these mutants without reinstating active zone networks. Re-expression of RIM zinc fingers recruited Munc13 to undocked vesicles and rendered the vesicles release-competent. Action potential-triggering of release was reconstituted by docking these primed vesicles to Ca^{2+} channels through attaching RIM zinc fingers to $Ca_V\beta4$-subunits. Our work identifies an 80-kDa β4-Zn protein that bypasses the need for megadalton-sized secretory machines, establishes that fusion competence and docking are mechanistically separable, and defines RIM zinc finger-Munc13 complexes as hubs for active zone function.

Graphical Abstract

*correspondence and lead contact: kaeser@hms.harvard.edu.

Author contributions

Conceptualization, C.T., S.S.H.W., and P.S.K.; Methodology, C.T., S.S.H.W., and G.d.N.; Formal Analysis, C.T., S.S.H.W., G.d.N. and P.S.K.; Investigation, C.T., S.S.H.W. and G.d.N.; Resources, C.T., S.S.H.W.; Writing-Original Draft, C.T. and P.S.K.; Writing-Review & Editing, C.T., G.d.N. and P.S.K.; Supervision, P.S.K.; Funding Acquisition, P.S.K.

Declaration of interests

The authors declare no competing interests. S.S.H.W. is currently an employee of RA Capital Management, LP.

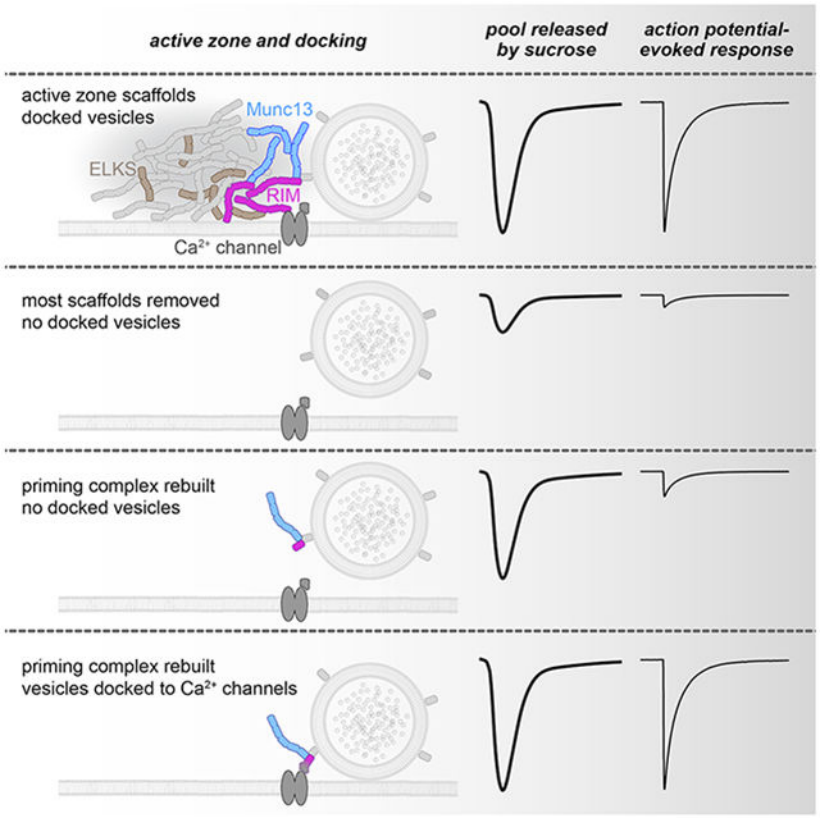

eTOC blurb

Presynaptic active zones are megadalton-sized protein machines for spatiotemporal precision of neurotransmitter release. Tan et al. ablate active zones and rebuild their functions within synapses using small protein domains. RIM zinc fingers rendered undocked vesicles fusion-competent, and Ca^{2+}-triggering of release was restored by tethering this priming domain to Ca^{2+} channels.

Introduction

Essential insight into the functioning of synaptic exocytotic machinery has come from rebuilding the fusion process in vitro. Reconstitution assays have revealed that the minimal machinery for Ca^{2+}-triggered exocytosis consists of SNARE proteins, Munc18, Munc13 and synaptotagmin (Hu et al., 2003; Ma et al., 2013; Tucker et al., 2004). However, fusion speed in these assays is orders of magnitude slower than at synapses, and spatial precision of exocytosis with its targeting towards postsynaptic receptor domains on target cells cannot be studied in these in vitro systems. These functions are carried out by the active zone, a molecular machine that is attached to the presynaptic plasma membrane and is composed of many megadalton-sized protein assemblies (Emperador-Melero and Kaeser, 2020; Südhof, 2012).

Central functions of the active zone are the generation of releasable vesicles and the positioning of these vesicles close to Ca^{2+} channels for rapid fusion-triggering (Augustin et al., 1999; Biederer et al., 2017; Deng et al., 2011; Imig et al., 2014; Kaeser et al., 2011;

Liu et al., 2011). Active zones are composed of families of scaffolding proteins including RIM, ELKS, Munc13, RIM-BP, Bassoon/Piccolo and Liprin-α (Südhof, 2012). Each protein family is encoded by multiple genes and the individual proteins are large, ranging from 125 to 420 kDa, forming complex protein networks. Understanding assembly mechanisms of these molecular machines remains a major challenge.

Gene knockout and related studies have uncovered loss-of-function phenotypes for individual active zone proteins. In essence, these studies established that each protein, in one way or another, participates in the control of each key exocytotic parameter. These parameters include: (1) the docking of vesicles (defined morphologically: the physical attachment of vesicles to the target membrane as assessed by electron microscopy), (2) the priming of vesicles (defined functionally: the production of release-competent vesicles through enhancing their fusogenicity), and (3) the coupling of these vesicles to Ca^{2+} channels (defined functionally: the releasability of primed vesicles in response to an action potential as a function of the distance of the primed vesicles to the source of Ca^{2+} entry). For example, roles in vesicle docking and priming have been described for RIM (Calakos et al., 2004; Deng et al., 2011; Han et al., 2011; Kaeser et al., 2011; Koushika et al., 2001), Munc13 (Aravamudan et al., 1999; Augustin et al., 1999; Deng et al., 2011; Imig et al., 2014; Richmond et al., 1999), Liprin-α (Emperador-Melero et al., 2021; Spangler et al., 2013; Wong et al., 2018), ELKS (Dong et al., 2018; Held et al., 2016; Kawabe et al., 2017; Matkovic et al., 2013), Piccolo/Bassoon (Parthier et al., 2018), and RIM-BP (Brockmann et al., 2019). Similarly, the control of Ca^{2+} secretion-coupling is mediated by the same proteins, with roles for RIM, RIM-BP, Bassoon, and ELKS (Acuna et al., 2015; Davydova et al., 2014; Dong et al., 2018; Grauel et al., 2016; Han et al., 2011; Kaeser et al., 2011; Kittel et al., 2006; Liu et al., 2014, 2011). A true mechanistic understanding of the active zone, however, has been difficult to achieve. This is in part because reconstitution assays, powerful for untangling mechanisms of the fusion reaction itself (Hu et al., 2003; Ma et al., 2013; Tucker et al., 2004), are not possible for the active zone due to its molecular complexity. Furthermore, the redundancy of scaffolding and release mechanisms has made it challenging to distinguish effects on active zone assembly from those on active zone function. Ultimately, it has not been possible to define which of the many candidate mechanisms at the active zone suffice to drive fast, action potential-triggered release.

Simultaneous conditional knockout of RIM and ELKS leads to disassembly of the active zone with loss of RIM, ELKS, RIM-BP, Piccolo, Bassoon and Munc13, a near-complete absence of vesicle docking, and a strong reduction in action-potential evoked exocytosis (Wang et al., 2016). General features of synaptic structure including the formation of boutons, the accumulation of vesicles, and the generation of synaptic contacts remain intact in these mutants. This has established that RIM and ELKS form a scaffolding complex that holds the active zone together.

Here, we use this active zone disruption through RIM+ELKS knockout to develop an approach for rebuilding hallmark functions of these secretory machines within synapses. Our overall goal was to develop a deep mechanistic understanding of active zone function and to define which of the many mechanisms are sufficient to drive release. We find that vesicles can be rendered release-competent by re-expression of RIM zinc fingers, which positioned

activated Munc13 on undocked vesicles. Docking of these vesicles next to Ca^{2+} channels was required to restore action potential-triggering of release. We achieved this using a single artificial fusion-protein consisting of the RIM zinc finger and the $Ca_V\beta$4-subunit, which resulted in recovery of fusion strength and speed after active zone disruption. These findings establish the minimal requirements for active zone function and define key protein domains sufficient to mediate these requirements.

Results

RIM restores structure and function at synapses with disrupted active zones

We first used stimulated emission depletion (STED) superresolution microscopy to evaluate active zone disruption induced by conditional knockout of RIM and ELKS, which strongly impaired extent and precision of neurotransmitter release (Wang et al., 2016). Cultured hippocampal neurons with floxed alleles for RIM1, RIM2, ELKS1 and ELKS2 were infected with cre-expressing lentiviruses to generate knockout (cKO^{R+E}) neurons or with control viruses to generate $control^{R+E}$ neurons. We then used a previously established workflow (Held et al., 2020; de Jong et al., 2018; Nyitrai et al., 2020; Wong et al., 2018) to assess active zone structure at 15-19 days in vitro (DIV). We identified side-view synapses in immunostainings by an elongated postsynaptic density (PSD, marked by PSD-95, STED) that was aligned with the edge of a synaptic vesicle cloud (Synaptophysin, confocal), and assessed localization of target proteins (STED) relative to these markers in line profiles (Figs. S1A-S1D). The cKO^{R+E} synapses had disrupted active zones with near-complete loss of ELKS2, RIM1 and Munc13-1, and strong reductions in Bassoon and RIM-BP2 (Figs. 1A-1K). In addition, we observed a partial loss of $Ca_V2.1$ (Figs. 1L, 1M), the α1-subunits of a major voltage-gated Ca^{2+} channel for release triggering at this synapse (Held et al., 2020). Removal of these active zone complexes, however, did not affect PSD-95 (Fig. 1C), and led to increases in Liprin-α3 (Figs. S1E, S1F), a protein that connects active zone assembly pathways to structural plasticity (Emperador-Melero et al., 2021; Wong et al., 2018).

With the overall goal to rebuild active zone function using the minimally required protein domains and interactions, we first tested whether either RIM or ELKS mediate recovery of active zone structure and function on their own. We re-expressed RIM1α or ELKS2αB, the main synaptic isoforms of the corresponding gene families (Kaeser et al., 2009, 2011; Liu et al., 2014; Schoch et al., 2002; Wang et al., 1997), using lentiviruses (Figs. 1A, S1G). We found that RIM1α was targeted correctly (Figs. 1B, 1C) and was able to re-establish normal levels and active zone positioning of Munc13-1, Bassoon, RIM-BP2, $Ca_V2.1$ and Liprin-α3 (Figs. 1F-1M, S1E, S1F). In contrast, re-expression of ELKS2αB did not lead to its localization to the target membrane area (Figs. 1D, 1E) and did not restore the localization of other proteins (Figs. 1F-1M, S1E, S1F), even though it was expressed efficiently (Fig. S1G). To assess protein levels upon rescue with an independent approach and to determine whether RIM-mediated active zone protein recruitment depends on RIM expression levels, we performed additional confocal microscopy experiments. Re-expression of lower or higher RIM1α levels using either a synapsin or ubiquitin promoter, respectively, mediated recovery of the other proteins dose-dependently. Higher levels of RIM1α were driving the recruitment of higher levels of Munc13-1, $Ca_V2.1$, and RIM-BP2 (Figs. S2A-

S2F). Higher synaptic levels of RIM1α also resulted in higher active zone levels of RIM1α (Figs. S2G, S2H). Altogether, these data indicate that RIM titrates levels of interacting proteins.

We next tested whether RIM1α re-expression restored key active zone functions, synaptic vesicle docking and release (Fig. 2). To assess synaptic ultrastructure, we fixed neurons with high pressure-freezing and analyzed electron microscopic images of synapses. Most cKO^{R+E} synapses lacked docked vesicles (assessed as vesicles for which the electron density of the vesicle membrane merges with that of the active zone target membrane), but other parameters including PSD length, bouton size and total vesicle numbers were unaffected. RIM1α restored vesicle docking to 51% of its initial levels, while ELKS2αB expression did not improve docking (Figs. 2A, 2B).

The active zone controls synaptic strength (sometimes also referred to as synaptic release probability), which is proportional to the product of the number of vesicles in the readily releasable pool (RRP), and the vesicular release probability p of each of these RRP vesicles. We measured synaptic strength and estimated these constituents, RRP and p, at excitatory and inhibitory synapses using electrophysiology (Figs. 2C-2N). Vesicular release probability p is inversely correlated with to the ratio of release in response to paired pulses at short interstimulus intervals (Zucker and Regehr, 2002), and application of hypertonic sucrose was used to estimate the RRP (Kaeser and Regehr, 2017; Rosenmund and Stevens, 1996). RIM1α mostly restored excitatory (Figs. 2C-2H) and inhibitory (Figs. 2I-2N) synaptic strength, and both RRP and p were recovered to a large extent at both synapse types. In contrast, ELKS2αB had no rescue activity on its own, consistent with the STED and electron microscopy data. Excitatory evoked transmission was monitored via NMDA receptors (NMDARs) in most experiments to avoid confounding effects of network activity triggered by AMPA receptor (AMPAR) activation. Decreasing initial p by lowering extracellular Ca^{2+} or the use of low affinity NMDAR antagonists confirmed that paired pulse ratios provide an accurate estimate of changes in p as a consequence of genetic manipulations under our conditions (Fig. S3). Together, these data establish that RIM is an important presynaptic organizer for the control of active zone protein levels, positioning and function.

Re-expressed RIM zinc fingers localize to the synaptic vesicle cloud

For building a minimal recovery system, we next distinguished between RIM domains that mediate active zone targeting of RIM from those that are important for its functions in scaffolding other proteins and in mediating vesicle docking and release. We generated lentiviral constructs (Figs. 3A, 3B) in which we either deleted individual RIM domains (RIM1-ΔZn, -ΔPDZ, -ΔC_2A and -ΔC_2B) or that contained only one domain at a time (RIM1-Zn, -PDZ and -C_2B; the tested C_2A domain constructs were not efficiently expressed and hence C_2A domains could not be assessed in these experiments). cKO^{R+E} neurons were transduced with each individual virus for rescue, and each protein was expressed efficiently (Figs. S4A, S4B).

Assessment of RIM active zone targeting using STED line profile analyses revealed that the PDZ domain was necessary for RIM target membrane localization after active zone

disruption, as removing the PDZ domain abolished RIM active zone targeting (Figs. 3C, 3D). Other domain deletions did not decrease RIM localization. Removing the C_2A domain slightly enhanced RIM active zone levels (Fig. 3D). This could be because removing C_2A domains might enhance RIM expression, or because C_2A might suppress RIM active zone targeting. None of the tested single RIM domains was targeted to the plasma membrane opposed to the PSD (Figs. 3E, 3F). Hence, while multiple RIM domains need to cooperate for RIM active zone targeting, the RIM PDZ domain is essential for such targeting. It is noteworthy that in neurons lacking only RIM, most active zone proteins remain localized to synapses, the PDZ domain is not essential for RIM localization to nerve terminals, and RIM1-ΔPDZ can enhance neurotransmitter release (de Jong et al., 2018; Kaeser et al., 2011). In active zone disrupted cKO^{R+E} synapses, this redundancy is lost and the PDZ domain is essential (Figs. 3C, 3D). This loss of redundancy is further illustrated by the finding that RIM1α re-expression is not sufficient to restore all synaptic parameters, as docking and p are only partially recovered. Hence, the highly interconnected active zone protein networks rely on redundant scaffolding mechanisms that include ELKS (Held and Kaeser, 2018).

The RIM zinc finger alone, while not localized to the active zone, was enriched within nerve terminals (Figs. 3E, 3F). RIM1-Zn localization highly overlapped with the synaptic vesicle protein Synaptophysin, suggesting that this domain may be associated with vesicles when expressed on its own. Since the RIM zinc finger interacts with the vesicular GTPases Rab3 and Rab27 (Dulubova et al., 2005; Fukuda, 2003; Wang et al., 1997), it is likely that RIM1-Zn associates through these interactions with synaptic vesicles. The complementary protein fragment, a version of RIM that lacks the zinc finger domain termed RIM1-ΔZn, localized to the active zone area apposed to the PSDs (Figs. 3C, 3D), establishing that the zinc finger domain is not required for the synaptic delivery of RIM.

Re-expressed RIM zinc fingers recruit Munc13 to non-docked vesicles and enhance vesicle fusogenicity

The differential localization of RIM1-Zn (to vesicles) and RIM1-ΔZn (to the target membrane) may be related to their roles in release. Previous studies in RIM knockout synapses indicated that RIM zinc finger domains prime synaptic vesicles while the other domains tether Ca_V2 channels and interact with the target membrane for release triggering (Deng et al., 2011; de Jong et al., 2018; Kaeser et al., 2011). We tested these models by assessing the molecular roles (recruitment of Munc13 and Ca_V2s) and functional roles (priming, docking and releasing of vesicles) of RIM1-Zn and RIM1-ΔZn after active zone disruption.

Strikingly, RIM1-Zn co-recruited Munc13 in a pattern mimicking the widespread localization of RIM1-Zn (Figs. 4B, 4C). In contrast, RIM1-ΔZn, which contains the PDZ-, C_2A-, PxxP-, C_2B-domains, localized to the active zone area (Figs. 3A-3D), but was unable to enhance Ca_V2s or Munc13 (Figs. 4B-4E). This suggests that RIM1-Zn, which binds to Munc13 and Rab3 (Betz et al., 2001; Dulubova et al., 2005), recruits Munc13 to synapses, stabilizes it, and turns it into a protein associated with synaptic vesicles. We next analyzed high pressure-frozen neurons using electron microscopy from the same rescue conditions.

Both RIM1-Zn and RIM1-ΔZn lacked docking activity, and synaptic vesicles remained undocked (Figs. 4F, 4G). In conclusion, Munc13, a protein important for synaptic vesicle docking (Imig et al., 2014; Siksou et al., 2009), was not targeted to the presynaptic plasma membrane upon RIM1-Zn re-expression but was instead associated with the vesicle cloud. Recovering its presence in the nerve terminal was not sufficient to mediate docking.

Electrophysiological recordings revealed that RIM1-Zn and RIM1-ΔZn failed to restore action potential-triggered synaptic transmission and p at excitatory cKO^{R+E} synapses (Figs. 4H-4M), and only some rescue of these parameters was observed at inhibitory cKO^{R+E} synapses (Figs. S4C-S4H). This is different from rescue experiments after RIM knockout only (instead of cKO^{R+E}), where RIM1-ΔZn expression restores Ca^{2+} entry and mediates an increase in p (Deng et al., 2011; Kaeser et al., 2011). Hence, RIM C-terminal scaffolding domains need ELKS or N-terminal RIM sequences (Figs. 1 and 2) to execute their roles in release, but are sufficient to mediate target membrane localization of RIM (Figs. 3C, 3D).

RIM1-Zn, however, enhanced vesicle fusogenicity measured via application of hypertonic sucrose nearly as efficiently as full-length RIM1α (Figs. 4J, 4K, S4E, S4F). These data support the model that RIM zinc fingers activate Munc13 for vesicle priming by recruiting and monomerizing it via binding to Munc13 C_2A domains (Camacho et al., 2017; Deng et al., 2011) and – strikingly – this function can be executed on non-docked vesicles distant from the target membrane. These vesicles, however, were not accessible for action potential-triggering. We conclude that undocked vesicles can become release-competent by positioning activated Munc13 on them. Hence, Munc13 enhances fusogenicity even if it is not localized to release sites at the target membrane, and these “molecularly” primed vesicles do not need to be docked. This may explain why some priming remains when the active zone is disrupted and docking is abolished (Wang et al., 2016), as some Munc13 may be recruited to vesicles via direct interactions (Quade et al., 2019).

Docking of release-competent vesicles to Ca^{2+} channels restores fast release in the absence of active zone scaffolds

With the goal to selectively rebuild active zone mechanisms without restoring the vast scaffolding structure, we aimed at positioning the release-competent vesicles close to Ca^{2+} entry. We screened eight fusion-proteins of the RIM zinc finger domain to other proteins or protein fragments associated with the target membrane (Fig. S5A). Fusions with $Ca_V\beta$ Ca^{2+} channel subunits appeared to restore evoked transmission and release probability (Figs. S5B-S5E), suggesting that they may do so by co-localizing vesicle priming and Ca^{2+}-entry. We selected the fusion of the RIM1 zinc finger to $Ca_V\beta4$ (Fig. 5A, β4-Zn) for a full characterization because of its strong tendency to rescue. Endogenous $Ca_V\beta4$ is localized to active zones (Figs. S5F, S5G), and HA-tagged $Ca_V\beta4$ requires Ca_V2 channels for its active zone localization (Figs. S5H-S5K). β4-Zn was efficiently expressed (Fig. S5L) and concentrated in an elongated structure at the target membrane (Figs. 5A-5C). The β4-Zn protein recruited Munc13-1 to the target membrane (Figs. 5D, 5E), and also enhanced $Ca_V2.1$ active zone levels back to control levels (Figs. 5F, 5G). The effects on $Ca_V2.1$ were absent when $Ca_V\beta4$ or RIM1-Zn were expressed on their own. Importantly, β4-Zn did not restore levels of the active zone scaffolds Bassoon and RIM-BP2 (Figs. 5H-5K). Hence,

the $Ca_V\beta4$-fusion targets the priming-complex of the RIM zinc finger and Munc13 to Ca^{2+} channels in the absence of megadalton-sized scaffolding networks that consists of full-length RIM, ELKS, RIM-BP and Bassoon.

When we assessed these synapses using electron microscopy, we found that β4-Zn fully restored synaptic vesicle docking (Figs. 5L, 5M), and the rescue efficacy appeared more robust than that of full-length RIM1α (Figs. 2A, 2B). $Ca_V\beta4$ or RIM1-Zn alone did not enhance docking (Figs. 5L, 5M). In electrophysiological recordings, we detected a full recovery of excitatory synaptic transmission, measured either via NMDARs (Figs. 6A, 6B) or via AMPARs (Figs. 6C, 6D), and of inhibitory synaptic transmission (Figs. 6K, 6L). This included restoration of RRP (Figs. 6E, 6F, 6M, 6N) and p (Figs. 6I, 6J, 6O, 6P) back to levels indistinguishable from control^{R+E} neurons. We next recorded an array of additional parameters which are affected by RIM+ELKS knockout, including miniature excitatory postsynaptic currents (mEPSCs), the extracellular Ca^{2+}-dependence of release, its sensitivity to the slow Ca^{2+}-buffer EGTA, and pool sizes in response to 250, 500 or 1000 mM sucrose. In cKO^{R+E} neurons, mEPSC frequencies decreased, mEPSC rise times increased, but amplitudes and decay times remained unchanged (Figs. 6G, 6H, S6A-S6D). The finding that mEPSC amplitudes are not increased indicates that postsynaptic homeostatic adaptations are not induced in these mutants, similar to other knockouts with strong decreases in release (He et al., 2017; Held et al., 2020; Schoch et al., 2001). β4-Zn fully restored mEPSC frequencies and rise times back to control^{R+E} levels (Figs. 6G, 6H, S6C). β4-Zn also rescued the extracellular Ca^{2+}-dependence (Figs. S6E-S6G) and EGTA-sensitivity (Figs. S6H, S6I) of evoked release, and the response to various sucrose concentrations (Figs. S6J, S6K). Altogether, these data establish that functional defects induced by active zone disruption are fully restored by β4-Zn expression. β4-Zn recruits Munc13 and mediates vesicle docking close to Ca^{2+} channels for recovery of extent and temporal precision of release. $Ca_V\beta4$ or RIM1-Zn alone did not mediate these functions except for RRP recovery by RIM1-Zn (Figs. 4, S4, 6), and it is hence unlikely that β4-Zn rescue activity is due to enhancement of Ca^{2+} entry or RRP through β-subunits directly (Dolphin, 2012; Guzman et al., 2019). In summary, these data establish that vesicle docking close to Ca^{2+} channels enhances p of vesicles that are primed by RIM1-Zn and Munc13.

To test the overall model that β4-Zn restores synaptic strength through docking of release-competent vesicles close to Ca^{2+} channels, we introduced K144E+K146E point mutations into the RIM zinc finger domain of β4-Zn (generating β4-Zn$^{K144/146E}$). It was previously established that this mutation abolishes binding of the RIM zinc finger to Munc13 (Deng et al., 2011; Dulubova et al., 2005). β4-Zn$^{K144/146E}$ was efficiently expressed and localized to the active zone area of the plasma membrane (Figs. 7A-7C, S7A). Abolishing Munc13 binding in β4-Zn$^{K144/146E}$ resulted in a loss of Munc13-1 recruitment to the target membrane (Figs. 7D, 7E). While β4-Zn$^{K144/146E}$ was still sufficient to mediate some enhancement of $Ca_V2.1$ levels, it appeared less efficient than β4-Zn (Figs. 7F, 7G), quantitatively matching with the somewhat lower β4-Zn$_{K144/146E}$ active zone levels (Figs. 7B, 7C). Disrupting binding of β4-Zn to Munc13 completely abolished rescue of vesicle docking (Figs. 7H, 7I) and of synaptic strength, RRP and p at both excitatory (Figs. 7J-7O) and inhibitory (Figs. S7B-S7G) synapses. These data strongly support the model that β4-Zn restores exocytosis via recruitment of Munc13 and vesicle docking.

Directing Munc13 and vesicle tethering away from the active zone

Some of the mechanisms of β4-Zn might rely on the remaining active zone scaffolds, for example Liprin-α. To test whether β4-Zn can recruit Munc13-1 to Ca_V2 channels independent of these remaining scaffolds, we assessed localization of β4-Zn-mVenus and Munc13-1-tdTomato in transfected HEK293T cells with or without Cerulean-$Ca_V2.1$ (Fig. 8A, all transfections also contained untagged α2δ1 proteins). When $Ca_V2.1$ was present, β4-Zn and Munc13-1 were targeted to the cell periphery similar to $Ca_V2.1$ channels (Figs. 8B-8E). Hence, the docking complex of RIM zinc fingers and Munc13 can be attached to Ca^{2+} channels without co-expression of other active zone proteins. We next tested whether this complex is sufficient to tether vesicles on membranes other than the presynaptic plasma membrane. We mistargeted Cerulean-tagged RIM1-Zn to mitochondria by fusing it to the transmembrane region of the outer leaflet mitochondrial protein Tom20 (Kanaji et al., 2000; Nyitrai et al., 2020) to generate mitoC-Zn, and used mito-Cerulean (mitoC) as a control (Fig. 8F). Lentiviral transduction of cKO^{R+E} neurons resulted in robust mitoC-Zn and mitoC expression and the proteins localized to mitochondria (Figs. S8A and S8B). MitoC-Zn enhanced Munc13-1 levels measured in mitochondrial ROIs (Figs. 8G, 8H), suggesting that the mitochondrial-targeted RIM zinc finger is sufficient to recruit Munc13-1 to mitochondria. Moreover, mitoC-Zn increased the tethering of vesicles to the surface of axonal mitochondria (Figs. 8I-8K) as assessed in electron microscopy. Synaptic ultrastructure and vesicle docking were unaltered by mitoC or mitoC-Zn compared to cKO^{R+E} in the same neurons (Figs. S8C, S8D). Hence, targeting of RIM1-Zn to mitochondria is sufficient to recruit Munc13-1 and to tether some vesicles to these mitochondria.

Discussion

The active zone is a molecular machine that is important for synaptic signaling (Emperador-Melero and Kaeser, 2020; Südhof, 2012), and many brain disorders are associated with mutations in active zone proteins or defective active zone function (Benarroch, 2013; Bucan et al., 2009; Johnson et al., 2003; Krumm et al., 2015; O'Roak et al., 2012; Thevenon et al., 2013; Verhage and Sørensen, 2020). However, understanding its mechanisms and restoring its functions have remained challenging because of the molecular complexity. Here, we develop a reconstitution approach within a synapse after we remove active zone protein machinery. We find that synaptic strength and temporal precision of vesicle release can be restored by positioning the RIM zinc finger, a small protein domain that recruits the priming protein Munc13, to presynaptic Ca^{2+} channels. Our work further reveals that Munc13 is positioned with RIM zinc fingers even when the zinc finger is mistargeted to other cellular compartments: if RIM zinc fingers are localized to undocked vesicles, Munc13 is co-recruited and enhances fusogenicity of these vesicles; if it is targeted to Ca_V2 channels at the plasma membrane, Munc13 is tethered to these channels; if it is localized on mitochondria, these mitochondria can recruit Munc13 and some vesicles to their surface. Ultimately, our results establish that most active zone scaffolds can be bypassed with an 80 kDa β4-Zn protein that docks fusion-competent vesicles close to Ca^{2+} channels, and these vesicles can be rapidly released in response to action potentials (Figs. 8L-8N).

Flexible order of priming and docking as a vesicle is prepared for release

Our results mechanistically define the two fundamental presynaptic processes: vesicle fusogenicity can be generated by activated Munc13 independent of its active zone positioning, and Ca^{2+}-secretion coupling is mediated by docking of Munc13-associated synaptic vesicles next to Ca^{2+} channels. Past studies have discovered that these processes rely on many proteins, and each active zone protein has contributed to each active zone function (Acuna et al., 2015; Aravamudan et al., 1999; Augustin et al., 1999; Brockmann et al., 2019; Davydova et al., 2014; Deng et al., 2011; Dong et al., 2018; Emperador-Melero et al., 2021; Grauel et al., 2016; Held et al., 2016; Imig et al., 2014; Kaeser et al., 2011; Kawabe et al., 2017; Kittel et al., 2006; Koushika et al., 2001; Lipstein et al., 2013; Liu et al., 2014, 2011; Matkovic et al., 2013; Richmond et al., 1999; Schoch et al., 2002; Varoqueaux et al., 2002; Wong et al., 2018; Zarebidaki et al., 2020; Zhen and Jin, 1999). These findings reflect that the active zone is a complex protein network with built-in redundancy. Knockout studies may lead to alterations of the entire network and not necessarily reveal highly specific mechanisms of isolated proteins. Hence, it has been difficult to define which proteins and mechanisms drive vesicle priming, docking and release. Our approach establishes that these functions can be executed even if most of these proteins are removed. Vesicle priming can be mediated by the RIM zinc finger domain, which is sufficient to recruit, stabilize and activate Munc13. When this mechanism is positioned close to Ca^{2+} channels, release-triggering is restored.

Models of neurotransmitter release propose that vesicle docking either precedes vesicle priming or occurs simultaneously with it (Hammarlund et al., 2007; Imig et al., 2014, 2020; Rosenmund and Stevens, 1996; Schikorski and Stevens, 2001; Sudhof, 2004), and that Munc13 mediates both roles through the control of SNARE complex assembly (Basu et al., 2005; Imig et al., 2014; Ma et al., 2013; Siksou et al., 2009; Südhof, 2012). In view of this literature, it is surprising that vesicle priming, or fusogenicity, can be generated in the absence of docking (Fig. 4). This challenges the linear docking-priming model that relies on SNARE-complex assembly. Our data instead reveal that the generation of fusion-competent vesicles and vesicle docking are molecularly separable processes, and that vesicles away from the active zone can be activated for fusion. We propose that the rate limiting step is not SNARE-complex assembly, as this necessitates the coincidence of docking and priming, but instead the availability and activation of Munc13. This is supported by the observation that fusion-competent vesicles can be generated by positioning Munc13 on undocked vesicles (Figs. 3, 4), by the notion that some fusion-competent vesicles remain when Munc13 is displaced from the active zone (Wang et al., 2016), and by the finding that knockout of RIM, which is upstream of Munc13's role in vesicle priming, leads to strong impairments in RRP (Calakos et al., 2004; Deng et al., 2011; Han et al., 2011). While Munc13 mediates both synaptic vesicle docking and priming (Augustin et al., 1999; Imig et al., 2014; Varoqueaux et al., 2002), generating fusion competence and vesicle docking are separable, at least after disrupting active zone structure. We propose that, while many RRP vesicles are docked (Borges-Merjane et al., 2020; Imig et al., 2014, 2020; Schikorski and Stevens, 2001), the presence and activation of Munc13 embody the bottleneck for vesicle priming. Munc13-mediated SNARE complex-assembly may not be rate-limiting for vesicle release and may occur before or during fusion.

Streamlined active zone assembly bypasses the need for complex scaffolds

Mechanisms and hierarchy of active zone protein recruitment have remained difficult to establish. Our work reveals that the RIM PDZ domain is important for recruitment of RIM to the active zone, as removing it prevents RIM active zone targeting. Furthermore, our data indicate that RIM drives recruitment of presynaptic protein machinery. RIM re-expression restores levels of all other active zone proteins and of Ca^{2+} channels, and more RIM drives the presence of more Munc13, Ca^{2+} channels and other active zone proteins. Recent work proposed that liquid-liquid phase separation of RIM, RIM-BP and Ca_V2s mediates active zone assembly (Wu et al., 2019, 2021). Our work is consistent with this model, and indicates that phase condensation of RIM and RIM-BP into liquid droplets is not necessary for neurotransmitter release per se, as fusing the RIM zinc finger domain to $Ca_V\beta4$ restores release in the absence of most RIM and RIM-BP sequences necessary for phase condensation. In principle, it is possible that other liquid phases, which may or may not incorporate Ca_V2s, could be at play. In this context, it is interesting that Liprin-α3 levels at the active zone increase upon active zone disruption. Liprin-α undergoes phase condensation, and participates in the regulation of active zone structure (Emperador-Melero et al., 2021; McDonald et al., 2020). It is possible, and perhaps likely, that two phases compete or are in equilibrium with one another at a synapse, and that removing one enhances the other. This is supported by the enhanced presence of Liprin-α3 upon disruption of the active zone protein complex between RIM, ELKS, RIM-BP, Ca_V2s, Munc13 and Bassoon (Fig. 1). Conversely, at Liprin-α2/3 knockout synapses enhanced levels of Ca_V2 proteins are present (Emperador-Melero et al., 2021). RIM may link the two phases together or participate in both, as its active zone recruitment is decreased upon Liprin-α ablation.

The artificial β4-Zn fusion protein enhances Ca_V2 active zone levels together with restoring vesicle docking and release. Our experiments assess this for $Ca_V2.1$. The sequence and biochemical similarities of $Ca_V2.1$ and $Ca_V2.2$ and their functional redundancy make it likely that our findings apply to both channels (Cao et al., 2004; Held et al., 2020; Hibino et al., 2002; Kaeser et al., 2011), while roles of $Ca_V2.3$ may be distinct (Breustedt et al., 2003; Dietrich et al., 2003; Myoga and Regehr, 2011; Wu et al., 1999). One possibility is that vesicle docking stabilizes the Ca_V2 protein complex at active zones. This model is supported by the observation that abolishing the docking function of β4-Zn by preventing its binding to Munc13 appears to revert this effect partially. Another possibility is that β4-Zn enhances the delivery of Ca_V2s to the active zone, and that Munc13 binding is required for this function. Ultimately, our data may suggest that a stable release site contains a docked vesicle, that release sites that do not contain docked vesicles are subject to dynamic rearrangements, and that Ca_V2s of unoccupied release sites may be more mobile (Schneider et al., 2015). An alternative model is that Ca_V2s and exocytotic protein machinery such as Munc13 are in different proteins complexes (Rebola et al., 2019). In this model RIM proteins would participate in distinct assemblies: one may define secretory sites and contain at least RIM and Munc13 (Deng et al., 2011; Emperador-Melero et al., 2021; Reddy-Alla et al., 2017; Sakamoto et al., 2018; Tang et al., 2016), and another controls Ca^{2+} channel clustering and contains RIM, RIM-BP and Ca_V2s (Acuna et al., 2016; Held et al., 2020; Hibino et al., 2002; Kaeser et al., 2011; Kushibiki et al., 2019; Liu et al., 2011; Oh et al., 2021; Wu et al., 2019). In this model, proteins like RIM or ELKS could bridge the complexes, and our

reconstitution would account for both functions (Fig. 8L). Future studies should address these models.

In aggregate, our data suggest that the release machinery assembly requirements are remarkably simple: RIM zinc fingers recruit Munc13 to prime vesicles, and if positioned next to Ca_V2 channels, these vesicles can be rapidly and precisely released (Figs. 8L-8N). We propose that synaptic strength is mainly determined through reconstituting these key mechanisms, and that other proteins mediate regulatory functions. Some secretory systems, for example those for striatal dopamine release, may make use of these relatively simple, streamlined mechanisms (Banerjee et al., 2021; Liu et al., 2018).

A small protein for rebuilding the function of a complex machine

Neurotransmitter secretion and sensing are often impaired in brain disease, ranging from highly specific associations of gene mutations in active zone proteins to more generalized breakdown of synaptic signaling, and these diseases are often called synaptopathies (Benarroch, 2013; Bucan et al., 2009; Johnson et al., 2003; Krumm et al., 2015; O'Roak et al., 2012; Thevenon et al., 2013; Verhage and Sørensen, 2020). Advances in AAV-based gene therapy strategies have spurred new hope for developing treatments for brain disorders (Hudry and Vandenberghe, 2019; Sun and Roy, 2021). However, a key limitation is that synaptic and secretory genes often exceed the packaging size of AAVs (Wu et al., 2010). A recent way to work past this limitation is the use of dual or triple AAVs that contain fragments and that are then spliced to generate whole proteins, for example for restoration of hearing (Akil et al., 2019; Al-Moyed et al., 2019). Another possibility is to find smaller proteins to restore function. Our reconstitution approach identifies a single 80 kDa-protein, the $Ca_V\beta4$-RIM zinc finger fusion, that is well within packaging limits of gene therapy viruses (Hudry and Vandenberghe, 2019; Wu et al., 2010). This relatively small protein can increase synaptic efficacy and is sufficient to mediate temporal precision of release after disrupting active zone architecture. Our approach serves as proof-of-concept for reconstructing functions of a complex molecular machine with relatively simple "pieces" by targeting these key elements to the right subcellular compartment.

STAR METHODS

Resource Availability

Lead contact.—Further information and requests for resources and reagents should be directed to and will be fulfilled by the Lead Contact, Pascal S. Kaeser (kaeser@hms.harvard.edu).

Materials availability.—Plasmids generated for this study will be shared without restrictions. Antibodies made in the Kaeser laboratory are exhaustible and will be shared as long as they are available. Mouse lines will be shared upon request within the limits of the respective material transfer agreements.

Data and code availability.—This study did not generate code. Data reported in this paper are available from the lead contact upon reasonable request. Any additional

information required to reanalyze the data reported in this paper is available from the lead contact upon request.

Experimental Model and Subject Details

Animals.—The quadruple homozygote floxed mice for RIM1αβ (Kaeser et al., 2008) (RRID: IMSR_JAX:015832, for ablation of the *Rims1* gene to remove RIM1α and RIM1β), RIM2αβγ (Kaeser et al., 2011) (RRID: IMSR_JAX:015833, for ablation of the *Rims2* gene to remove RIM2α, RIM2β and RIM2γ), ELKS1α (Liu et al., 2014) (RRID: IMSR_JAX:015830, for ablation of the *Erc1* gene to remove ELKS1αA and ELKS1αB) and ELKS2α (Kaeser et al., 2009) (RRID: IMSR_JAX:015831, for ablation of the *Erc2* gene to remove ELKS2αA and ELKS2αB) were previously described (Wang et al., 2016). Ca_V2 conditional triple homozygote floxed mice for $Ca_V2.1$ (Todorov et al., 2006), $Ca_V2.2$ (Held et al., 2020), and $Ca_V2.3$ (Pereverzev et al., 2002) mice were previously described (Held et al., 2020). The genotype of all mice was homozygote floxed for the corresponding alleles. Mice were housed as breeding pairs or separated by sex (up to 5 adult mice per cage) in a 12 h light-dark cycle with free access to food and water, in a room dedicated to mouse breeding set to 22 °C (range 20-24 °C) and 50% humidity (range 35-70%). Experiments were performed on cultured primary neurons from postnatal day 0 male and female newborns of these mice. All animal experiments were performed according to institutional guidelines at Harvard University.

Primary cultures.—Primary mouse hippocampal cultures were generated from newborn mice as described before (Held et al., 2020; Wang et al., 2016), and cells from mice of both sexes were mixed. Within 24 h after birth, mice were anesthetized on ice slurry, euthanized by decapitation, and the hippocampi were dissected out. Cells were dissociated and plated onto glass coverslips in tissue culture medium composed of Minimum Essential Medium (MEM) with 0.5% glucose, 0.02% $NaHCO_3$, 0.1 mg/mL transferrin, 10% Fetal Select bovine serum (Atlas Biologicals FS-0500-AD), 2 mM L-glutamine, and 25 μg/mL insulin. Cultures were maintained in a 37 °C-tissue culture incubator, and after ~24 h the plating medium was exchanged with growth medium composed of MEM with 0.5% glucose, 0.02% $NaHCO_3$, 0.1 mg/mL transferrin, 5% Fetal Select bovine serum (Atlas Biologicals FS-0500-AD), 2% B-27 supplement (Thermo Fisher 17504044), and 0.5 mM L-glutamine. At DIV3 or DIV4, depending on growth, 50% or 75% of the medium were exchanged with growth medium supplemented with 4 μM Cytosine β-D-arabinofuranoside (AraC) to inhibit glial cell growth. Analyses were performed at DIV15-19 as described below.

Cell lines.—HEK293T cells, an immortalized cell line of female origin, were purchased from ATCC (CRL-3216, RRID: CVCL_0063), expanded, and stored in liquid nitrogen until use. After thawing, the cells were grown in Dulbecco's Modified Eagle Medium (DMEM) with 10% Fetal bovine serum (Atlas Biologicals F-0500-D) and 1% Penicillin-Streptomycin. HEK293T cells were passaged every 2-3 d at a ratio of 1:5 to 1:7. HEK293T cell batches were typically replaced after 20 passages by thawing a fresh vial from the expanded stock.

Method Details

Lentiviruses.—Lentiviruses were used to transduce primary hippocampal neurons. Lentiviruses expressing EGFP-tagged cre recombinase (to generate cKO^{R+E} neurons, made using pFSW EGFP cre) or a truncated, enzymatically inactive EGFP-tagged cre protein (to generate $control^{R+E}$ neurons, made using pFSW EGFP Δcre) were produced in HEK293T cells by Ca^{2+} phosphate transfection. Protein expression from these lentiviruses was driven by a human synapsin promoter to restrict expression to neurons (Liu et al., 2014; Wang et al., 2016) except for the $RIM1\alpha_{high}$ condition (which was done using FUGW RIM1α-HA with a ubiquitin promoter). For cre-expressing and control virus, neurons were infected with HEK cell supernatant at DIV5 as described (Liu et al., 2014; Wang et al., 2016). For expression of various proteins (ELKS1αB, ELKS2αB, RIM1α, RIM1 mutants, $Ca_V\beta4$, β4-Zn, mitoC, mitoC-Zn and other RIM1-Zn fusion constructs), neurons were infected with lentivirus for expression of these proteins at DIV3 (a virus made using pFSW without a cDNA inserted in the multiple cloning site was used in the control conditions instead of an expression virus) and with cre or Δcre virus at DIV5 unless noted otherwise. For experiments with Ca_V2 ablation, neurons were infected with cre or Δcre virus at DIV1 and with $Ca_V\beta4$-expressing virus at DIV3. For experiments with mitoC and mitoC-Zn expression in neurons, neurons were also infected with a lentivirus expressing mito-DsRed at DIV7 to label mitochondria.

Rescue and other constructs.—For full-length RIM1α (all residue numbering is according to Uniprot ID Q9JIR4), the open reading frame was subcloned into lentiviral backbones and expression was driven by either a synapsin promoter (pFSW RIM1α-HA, p592) for lower expression or a ubiquitin promoter (pFUGW RIM1α-HA, p591, described in (de Jong et al., 2018)) for higher expression. The synapsin promoter was used in all other rescue constructs. For all experiments, RIM zinc finger refers to residues (in single letter code) M1-D213, RIM PDZ to H597-R705, RIM C_2A to Q754-Q882, and RIM C_2B to G1447-S1615. All RIM1 individual domains (pFSW RIM1-Zn-HA, p654; pFSW RIM1-PDZ-HA, p648; pFSW RIM1-C2B-HA, p647) and domain deletion mutants (pFSW RIM1-ΔZn-HA, p640; pFSW RIM1-ΔPDZ-HA, p639; pFSW RIM1-ΔC2A-HA, p637; pFSW RIM1-ΔC2B-HA, p638) span or lack these residues, except for the pFSW RIM1-ΔZn-HA, which spans H597-S1615. In RIM1α and in domain deletion mutants, an HA-tag was inserted between residues E1379-S1380. In RIM1 individual domains, an HA-tag was inserted at the C-terminus. The splice variant of full-length RIM1α was lacking alternatively spliced exons (N83-W105, H1084-R1169, A1207-T1378) identical to previous experiments (Deng et al., 2011; de Jong et al., 2018; Kaeser et al., 2011; Tang et al., 2016). For pFSW HA-ELKS1αB (p311) and pFSW HA-ELKS2αB (p314), an HA-tag was inserted at the N-terminus (Held et al., 2016; Nyitrai et al., 2020). The plasmids for expression of zinc finger fusion-proteins were newly generated based on the following cDNAs: pMT2 $Ca_V\beta1b$ GFP (gift from Annette Dolphin obtained through Addgene, plasmid # 89893; http://addgene.org/89893; RRID:Addgene_89893 (Page et al., 2016)), Cavβ3 (gift from Diane Lipscombe; http://addgene.org/26574 RRID:Addgene_26574) and pMT2 $Ca_V\beta4$ (gift from Annette Dolphin obtained through Addgene, plasmid # 107426; http://addgene.org/107426; RRID:Addgene_107426 (Page et al., 2016)). The cDNAs of Liprin-α3 (Wong et al., 2018), $Ca_V2.1$ (Held et al., 2020) and $RIM1\text{-}Zn^{K144/146E}$ (Deng et al., 2011) were described

before. For pFSW β4-Zn-HA (p661), an HA-tag followed by RIM1-Zn was inserted at the C-terminus of $Ca_V\beta4$, with the stop codon in $Ca_V\beta4$ and start codon in RIM1-Zn deleted. For all other RIM1-Zn fusion-proteins, similar strategies were used as shown in Fig. S5A. For pFSW Tom20-Cerulean-Zn (p666, termed mitoC-Zn), a mito-tag composed of the transmembrane domain of the mitochondrial Tom20 protein (Kanaji et al., 2000) and a Cerulean fluorescent protein (pFSW Tom20-Cerulean, p049 (Nyitrai et al., 2020), termed mitoC) was fused onto the N-terminus of RIM1-Zn.

STED imaging.—Neurons cultured on 0.17 mm thick 12 mm diameter (#1.5) coverslips were washed two times with warm PBS, and then fixed in 4% PFA for 10 min unless noted otherwise. For $Ca_V2.1$ staining, cultures were fixed in 2% PFA + 4% sucrose (in PBS) for 10 min. After fixation, coverslips were rinsed twice in PBS + 50 mM glycine, then permeabilized in PBS + 0.1% Triton X-100 + 3% BSA (TBP) for 1 h. Primary antibodies were diluted in TBP and stained for 24-48 h at 4 °C. The following primary antibodies were used: guinea pig anti-Synaptophysin (1:500, RRID: AB_1210382, A106), mouse anti-PSD-95 (1:200, RRID: AB_10698024, A149, knockout-verified according to vendor), rabbit anti-RIM1 (1:500, RRID: AB_887774, A58, knockout-verified in lab), rabbit anti-ELKS2α (serum E3-1029, 1:100, custom made, A136, (Held et al., 2016), knockout-verified in lab), rabbit anti-Munc13-1 (1:500, RRID: AB_887733, A72, knockout-verified in lab), rabbit anti-$Ca_V2.1$ (1:200, RRID: AB_2619841, A46, knockout-verified in lab), rabbit anti-RIM-BP2 (1:500, RRID: AB_2619739, A126, knockout-verified in lab), rabbit anti-Liprin-α3 (serum 4396, 1:2000, gift from Dr. T. Südhof, A35, knockout-verified in lab), rabbit anti-Synaptophysin (1:500, RRID: AB_887905, A64), guinea pig anti-$Bassoon^C$ (C-terminal, 1:500, RRID: AB_2290619, A67) and mouse anti-HA (1:500, RRID: AB_2565006, A12, verified in the absence of antigen in lab). After primary antibody staining, coverslips were rinsed twice and washed 3-4 times for 5 min in TBP. Alexa Fluor 488 (anti-guinea pig, RRID: AB_2534117, S3; anti-rabbit, RRID: AB_2576217, S5; anti-mouse IgG1, RRID: AB_2535764, S7), 555 (anti-mouse IgG2a, RRID: AB_1500824, S20), and 633 (anti-rabbit, RRID: AB_2535731, S33; anti-guinea pig, RRID: AB_2535757, S34) conjugated antibodies were used as secondary antibodies at 1:200 (Alexa Fluor 488 and 555) or 1:500 (Alexa Fluor 633) dilution in TBP, incubated for 24 h at 4 °C followed by rinsing two times and washing 3-4 times 5 min in TBP. Stained coverslips were post-fixed for 10 min with 4% PFA in PBS (for $Ca_V2.1$ staining, 4% PFA + 4% sucrose in PBS was used for post-fixation), rinsed two times in PBS + 50 mM glycine and once in deionized water, and air-dried and mounted on glass slides. STED images were acquired with a Leica SP8 Confocal/STED 3X microscope with an oil immersion 100x 1.44 numerical aperture objective and gated detectors as described in (Wong et al., 2018); 46.51 x 46.51 μm^2 areas were acquired (4096 x 4096 pixels, 11.358 nm/pixel). Alexa Fluor 633, Alexa Fluor 555, and Alexa Fluor 488 were excited with 633 nm, 555 nm and 488 nm using a white light laser at 2-5% of 1.5 mW laser power. The Alexa Fluor 633 channel was acquired first in confocal mode using 2x frame averaging. Subsequently, Alexa Fluor 555 and Alexa Fluor 488 channels were acquired in STED mode, depleted with 660 nm (50% of max power, 30% axial depletion) and 592 nm (80% of max power, 30% axial depletion) depletion lasers, respectively. Line accumulation (2-10x) and frame averaging (2x) were applied during STED scanning. Identical settings were applied to all samples within an experiment. Synapses within STED images were

selected in side-view, defined as synapses that contained a synaptic vesicle cluster labeled with Synaptophysin and associated with an elongated PSD-95 structure along the edge of the vesicle cluster as described (Held et al., 2020; de Jong et al., 2018; Nyitrai et al., 2020; Wong et al., 2018). For intensity profile analyses, side-view synapses were selected using only the PSD-95 signal and the vesicle signal for all experiments. An ROI was manually drawn around the PSD-95 signal and fit with an ellipse to determine the center position and orientation. A ~1200 nm long, 200 nm wide rectangle was then selected perpendicular and across the center of the elongated PSD-95 structure. Intensity profiles were obtained for all three channels within this ROI. To align individual profiles, the PSD-95 signal only was smoothened using a moving average of 5 pixels, and the smoothened signal was used to define the peak position of PSD-95. All three channels (vesicle marker, test protein, and smoothened PSD-95) were then aligned to the PSD-95 peak position and averaged across images. All analyses were performed on raw images without background subtraction, and all adjustments and were done identically for all experimental conditions. Here (Fig. S2) and in previous analyses (Wong et al., 2018), levels analyzed with STED microscopy correlate well with those analyzed in confocal microscopy (see below) despite the non-linearities that may be present in these methods. Representative images in figures were brightness and contrast adjusted to facilitate inspection, and these adjustments were made identically for images within an experiment. The experimenter was blind to the condition/genotype for image acquisition and analyses.

Confocal imaging of cultured neurons.—Neurons cultured on glass coverslips were washed with warm PBS and fixed in PFA for 20 min. Neurons were then permeabilized in TBP for 1 h, and then incubated in primary antibodies at 4 °C overnight. The following primary antibodies were used: rabbit anti-RIM1 (1:1000, RRID: AB_887774, A58, knockout-verified in lab), rabbit anti-ELKSα (1:500, RRID: AB_869944, A55, knockout-verified in lab), rabbit anti-Munc13-1 (1:500, RRID: AB_887733, A72, knockout-verified in lab), rabbit anti-$Ca_V2.1$ (1:1000, RRID: AB_2619841, A46, knockout-verified in lab), rabbit anti-RIM-BP2 (1:500, RRID: AB_2619739, A126, knockout-verified in lab), mouse anti-Bassoon (1:500, RRID: AB_11181058, A85), mouse anti-MAP2 (1:500, RRID: AB_477193, A108), rabbit anti-MAP2 (1:1000, RRID: AB_2138183, A139), guinea pig anti-Synaptophysin (1:500, RRID: AB_1210382, A106), rabbit anti-GFP (1:500, RRID: AB_591816, A211). After staining with primary antibodies, coverslips were rinsed twice and washed 3-4 times for 5 min in TBP. Alexa Fluor 488 (for detection of the protein of interest, anti-rabbit, RRID: AB_2576217, S5; anti-mouse IgG1, RRID: AB_2535764, S7), 546 (for detection of MAP2, anti-mouse IgG, RRID: AB_2535765, S12; anti-rabbit, RRID: AB_2534093, S16), and 633 (for detection of Synaptophysin, anti-guinea pig, RRID: AB_2535757, S34) conjugated secondary antibodies were used at 1:500 dilution in TBP. Secondary antibody staining was done for 2 h at room temperature followed by rinsing two times and washing 3-4 times 5 min in TBP. Coverslips were rinsed once with deionized water and mounted on glass slides. Images were taken on an Olympus FV1200 confocal microscope with a 60x oil-immersion objective or on a Leica SP8 Confocal/STED 3X microscope with a 63x oil-immersion objective using identical settings per condition in a given experiment and single confocal sections were analyzed in ImageJ. For quantitative analyses of synaptic protein levels and mitochondrial Munc13-1 levels, the Synaptophysin-

or DsRed-signals were used to define ROIs, respectively. The signal intensity of the protein of interest was quantified within these ROIs. For each image, the “rolling ball” ImageJ plugin was set to a diameter of 1.4 μm for local background subtraction (Sternberg, 1983). Representative images in figures were brightness and contrast adjusted to facilitate inspection, and adjustments were made identically across conditions. The experimenter was blind to the condition/genotype for image acquisition and analyses.

Confocal imaging in transfected HEK293T cells.—For confocal analyses of $Ca_V2.1$, β4-Zn and Munc13-1 staining in HEK293T cells, cells were plated on matrigel-coated glass coverslips (12 mm in diameter) at 10-20% confluency in 12-well plates. 24 h later, cells were co-transfected with pcDNA α2δ1 (p752), pCMV β4-Zn-mVenus (p910) and pcDNA Munc13-1-tdTomato (p888) with or without pCMV Cerulean-$Ca_V2.1$ (p773) at 1:1:1(:1) molar ratio with a total of 347 (500 ng) of DNA per well per well. 24 h after transfection, the cells were washed with warm PBS and fixed in 4% PFA in PBS for 10 min. Coverslips were rinsed once with deionized water and mounted onto glass slides for imaging of fluorophores without additional staining. Images were taken using identical settings per condition on a Leica SP8 Confocal/STED 3X microscope with a 63x oil-immersion objective and single confocal sections were analyzed in ImageJ. Based on the localization of Cerulean-$Ca_V2.1$, a 1 μm-thick ROI was set along the outer edge of the cell (edge), and the enclosed area was defined as the inside of the cell (inside). The average intensity within the edge ROI and inside ROI was quantified and the edge:inside ratio was calculated for each cell. Representative images in figures were brightness and contrast adjusted to facilitate inspection, and these adjustments were made identically for images within an experiment. The experimenter was blind to the condition for image acquisition and analyses.

Electrophysiology.—Electrophysiological recordings in cultured hippocampal neurons were performed as described (Held et al., 2020; Liu et al., 2014; Wang et al., 2016) at DIV15-19. Glass pipettes were pulled at 2 - 5 MΩ and filled with intracellular solutions containing (in mM) for EPSC recordings: 120 Cs-methanesulfonate, 2 $MgCl_2$, 10 EGTA, 4 Na_2-ATP, 1 Na-GTP, 4 QX314-Cl, 10 HEPES-CsOH (pH 7.4, ~300 mOsm) and for IPSC recordings: 40 CsCl, 90 K-gluconate, 1.8 NaCl, 1.7 $MgCl_2$, 3.5 KCl, 0.05 EGTA, 2 Mg-ATP, 0.4 Na_2-GTP, 10 phosphocreatine, 4 QX314-Cl, 10 HEPES-CsOH (pH 7.2, ~300 mOsm). Cells were held at +40 mV for NMDAR-EPSC recordings and at −70 mV for AMPAR-EPSC, mEPSC, sucrose EPSC, IPSC and sucrose IPSC recordings. Access resistance was monitored during recordings and compensated to 3-5 MΩ, and cells were discarded if the uncompensated access exceeded 15 MΩ. The extracellular solution contained (in mM): 140 NaCl, 5 KCl, 2 $MgCl_2$, 1.5 $CaCl_2$, 10 glucose, 10 HEPES-NaOH (pH 7.4, ~300 mOsm), the $CaCl_2$ concentration was 0.5 mM instead of 1.5 mM for Figs. S3A-S3D, all recordings were performed at room temperature (20-24 °C). To assess action potential-triggered excitatory transmission, NMDAR-mediated excitatory postsynaptic currents (NMDAR-EPSCs) were measured to avoid network activity induced by AMPA receptor activation unless noted otherwise. For NMDAR-EPSCs, picrotoxin (PTX, 50 μM) and 6-Cyano-7-nitroquinoxaline-2,3-dione (CNQX, 20 μM) were present in the extracellular solution, for Figs. S3E-S3H, 20 μM L-AP5 was added to the extracellular solution. For AMPAR-EPSCs, D-amino-5-phosphonopentanoic acid (D-APV, 50 μM) and

PTX (50 μM) were present in the extracellular solution; 1 mM γ-D-Glutamylglycine (γ-DGG) was also added to the bath to prevent AMPAR saturation, which also reduced the reverberant activity that is present upon electrical stimulation. Inhibitory postsynaptic currents (IPSCs) were recorded in the presence of D-APV (50 μM) and CNQX (20 μM) in the extracellular solution. Action potentials were elicited with a bipolar focal stimulation electrode fabricated from nichrome wire. Paired pulse ratios were calculated as the amplitude of the second PSC divided by the amplitude of the first at each interval from an average of 6 sweeps per cell and interval. The baseline value for the second PSC was taken immediately after the second stimulus artifact. For dependence of IPSC amplitudes on the extracellular Ca^{2+} concentration ($[Ca^{2+}]_{ex}$), neurons were perfused with solutions containing 0.5/3.5, 1/3, 2/2, 5/0.25, 10/0.25 mM $[Ca^{2+}]_{ex}/[Mg^{2+}]_{ex}$ in variable order. Recordings began at 0.5 mM $[Ca^{2+}]_{ex}$/3.5 mM $[Mg^{2+}]_{ex}$ and for each solution exchange, five chamber volumes of solution were replaced. Only cells in which all five $[Ca^{2+}]_{ex}$ were recorded were included in the analysis. For the normalized data, IPSC amplitudes for each cell were normalized to the same cell's amplitude at 10 mM $[Ca^{2+}]_{ex}$/0.25 mM $[Mg^{2+}]_{ex}$. The absolute and normalized data were fit to the Hill equation $I = I_{min} + ([Ca^{2+}]_{ex}\text{^HillSlope}) * (I_{max} - I_{min}) / ([Ca^{2+}]_{ex}\text{^HillSlope} + EC_{50}\text{^HillSlope})$. For EGTA-dependence of IPSCs, 100 μM EGTA-AM in DMSO (final DMSO 0.33% of total volume), or DMSO only as control, was added to the media and the neurons were incubated for 10 min in a 37 °C tissue culture incubator. The neurons were then transferred from culture medium to extracellular solution and recorded as described above. For normalization, four to five cells incubated with DMSO only were recorded for each genotype in each culture, and the IPSCs in EGTA-AM were normalized to the average of these control cells per genotype and culture. For mEPSC recordings and sucrose-induced EPSC recordings, TTX (1 μM), PTX (50 μM), and D-APV (50 μM) were added to the extracellular solution, and for sucrose-induced IPSC recordings, TTX (1 μM), CNQX (20 μM), and D-APV (50 μM) were added. mEPSC were identified with a template search followed by manual confirmation by an experimenter, and their frequencies were assessed during a 100-s recording time window after stabilizing the baseline for 3-min after break-in. mEPSC amplitudes and mEPSC kinetics were determined for each cell by averaging the waveform of all events identified during the 100-s recording time window aligned to the beginning of the events. Rise times were measured as the time interval between 20% and 80% of the peak amplitude and decay τ as the interval from 100% to 37% of the decay phase. The RRP was estimated by application of 500 mM sucrose in extracellular solution applied via a microinjector syringe pump for 10 s at a rate of 10 μl/min through a tip with an inner diameter of 250 μm. For sucrose concentration-dependence, solutions with 250 mM, 500 mM or 1000 mM sucrose (in extracellular solution) were used. Data were acquired at 5 kHz and lowpass filtered at 2 kHz with an Axon 700B Multiclamp amplifier and digitized with a Digidata 1440A digitizer. All data acquisition and analyses were done using pClamp10. For electrophysiological experiments, the experimenter was blind to the genotype throughout data acquisition and analysis.

High-pressure freezing and electron microscopy.—Neurons cultured on 6 mm matrigel-coated sapphire coverslips were frozen using a Leica EM ICE high-pressure freezer in extracellular solution containing (in mM): 140 NaCl, 5 KCl, 2 $MgCl_2$, 2 $CaCl_2$, 10 HEPES-NaOH (pH 7.4), 10 Glucose (~300 mOsm) with CNQX (20 μM), D-AP5 (50 μM)

and PTX (50 μM) added to block synaptic transmission. After freezing, samples were first freeze-substituted (AFS2, Leica) in 1% glutaraldehyde, 1% osmium tetroxide, 1% water in anhydrous acetone as follows: −90 °C for 5 h, 5 °C per h to −20 °C, −20 °C for 12 h, and 10 °C per h to 20 °C. Following freeze substitution, samples were Epon infiltrated, and baked for 48 h at 60 °C followed by 80 °C overnight before sectioning at 50 nm. For ultrathin sectioning, the sapphire coverslip was removed from the resin block by plunging the sample first in liquid nitrogen and followed by warm water several times until the sapphire was completely detached. The resin block containing the neurons was then divided into four pieces, and one piece was mounted for sectioning. Ultrathin sectioning was performed on a Leica EM UC7 ultramicrotome, and the 50 nm sections were collected on a nickel slot grid (2 x 1 mm) with a carbon coated formvar support film. The samples were counterstained by incubating the grids with 2% lead acetate solution for 10 s, followed by rinsing with distilled water. Images were taken with a transmission electron microscope (JEOL 1200 EX at 80 kV accelerating voltage) and processed with ImageJ. The total number of vesicles, the distance of individual vesicles to the active zone area of the presynaptic membrane (defined by apposition to the PSD), the number of docked vesicles per synapse profile, the length of the PSD, and the area of the presynaptic bouton were analyzed in each section using a custom-written Matlab code. Bouton size was calculated from the measured perimeter of each synapse. Docked vesicles per active zone were defined as vesicles touching the presynaptic plasma membrane opposed to the PSD, and only vesicles for which the electron densities of the vesicular membrane and the presynaptic plasma membrane merged such that they were not separated by less electron dense space were considered docked. We also measured vesicle distribution within 100 nm from the presynaptic membrane in 10 nm bins. Across experiments, only vesicle distribution in 0-10 nm was altered within the first 100 nm depending on genotype/manipulation, largely reflecting changes in docked vesicles as defined above. We show vesicle distribution as an inset for the first electron microscopic experiment (Fig. 2B), but only report docked vesicles for subsequent experiments for simplicity. Due to the laborious nature of these experiments, it was not possible to include a RIM1α full-length rescue condition in each experiment. Instead, we always included control^{R+E} and cKO^{R+E} neurons as essential controls for comparison. For assessment of vesicles tethered to mitochondria, the number of small vesicles (diameter < 50 nm) associated with the mitochondrial surface was counted. A vesicle was considered tethered if it was within 70 nm from a mitochondrial surface, as this was the longest tether that we visually identified previously (Nyitrai et al., 2020). The number of vesicles was normalized to the mitochondrial perimeter (μm) for each mitochondrion. Experiments and analyses were performed by an experimenter blind to the genotype.

Western blotting.—For assessment of rescue protein expression in cultured neurons, Western blotting was used to detect target proteins in cell lysates from select coverslips of every culture that was used for electrophysiology or electron microscopy. At DIV15-19, cultured neurons were harvested in 20 μl 1x SDS buffer per coverslip and run on standard SDS-Page gels followed by transfer onto nitrocellulose membranes. Membranes were blocked in filtered 10% nonfat milk/5% goat serum for 1 h at room temperature and incubated with primary antibodies in 5% nonfat milk/2.5% goat serum overnight at 4 °C, and HRP-conjugated secondary antibodies (1:10,000, anti-mouse, RRID: AB_2334540;

anti-rabbit, RRID: AB_2334589) were used. Anti-Synapsin or -β-actin antibodies were used as loading controls. The following primary antibodies were used: rabbit anti-RIM1 (1:1000, RRID: AB_887774, A58, knockout-verified in lab), rabbit anti-ELKS2αB (1:500, RRID: AB_731499, A143, knockout-verified in lab), rabbit anti-RIM1-Zn (1:500, gift from Dr T. Südhof, A148, knockout-verified in lab), mouse anti-HA (1:1000, RRID: AB_2565006, A12, verified in the absence of antigen in lab), mouse anti-Synapsin (1:4000, RRID: AB_2617071, A57, knockout-verified according to vendor), rabbit anti-GFP (1:2000, RRID:AB_2636878, A146), mouse anti-β-actin (1:2000, RRID: AB_476692, A127), mouse anti-$Ca_V\beta4$ (1:50, RRID: AB_10671176, A123). For illustration in figures, images were adjusted for brightness and contrast to facilitate visual inspection.

Quantification and Statistical Analysis

Data are displayed as mean ± SEM. Statistics were performed in GraphPad Prism 9, and significance is presented as * $P < 0.05$, ** $P < 0.01$, and *** $P < 0.001$. Sample sizes and statistical tests for each experiment are included in each figure legend. For electrophysiological experiments, the sample size used for statistical analyses was the number of recorded cells. For STED microscopic and electron microscopic data, the sample size used for statistical analyses was the number of synapses except for Figs. 8I-8K, where it was the number of mitochondria. For confocal microscopic data, the sample size used for statistical analyses was the number of analyzed ROIs, which corresponds to the number of images (Figs. S2A-S2F, 8F-8H) or the number of cells (Figs. 8A-8E). Parametric tests were used for normally distributed data (assessed by Shapiro-Wilk tests) or when sample size was $n \geq 30$. One-way ANOVA followed by Dunnett's multiple comparisons post-hoc tests were used for datasets with equal variance. When variances were unequal, Welch's unequal variances t-test, Brown-Forsythe ANOVA followed by Games-Howell's multiple comparisons post hoc tests (for $n \geq 50$) or Dunnett's T3 multiple comparisons post hoc tests (for $n < 50$) were used. For non-normally distributed data, nonparametric tests were used (Mann-Whitney tests or Kruskal-Wallis tests followed by Dunn's multiple comparisons post-hoc tests). For paired pulse ratios, two-way ANOVA with Dunnett's tests was used. For STED side-view analyses, two-way ANOVA with Dunnett's tests was used on a 200 nm-window centered around the active zone peak. For each dataset, the specific tests used are stated in the figure legends.

Supplementary Material

Refer to Web version on PubMed Central for supplementary material.

Acknowledgments

We thank J. Wang and C. Qiao for technical support, E. Raviola, W. Regehr, R. Held and H. Nyitrai for insightful discussions and help with setting up experimental approaches, all members of the Kaeser laboratory for feedback, M. Verhage and J. Broeke for a MATLAB macro to analyze electron microscopic images, A.M.J.M. van den Maagdenberg for $Ca_V2.1^{floxed}$ mice, and T. Schneider for $Ca_V2.3^{floxed}$ mice. This work was supported by grants from the NIH (R01MH113349 and R01NS083898 to P.S.K.), the Armenise Harvard Foundation (to P.S.K.), and an NSF graduate research fellowship (DGE1144152 to S.S.H.W.). We acknowledge the Neurobiology Imaging Facility (supported by a P30 Core Center Grant P30NS072030), and the Electron Microscopy Facility at Harvard Medical School.

References:

Acuna C, Liu X, Gonzalez A, and Südhof TC (2015). RIM-BPs Mediate Tight Coupling of Action Potentials to Ca(2+)-Triggered Neurotransmitter Release. Neuron 87, 1234–1247. [PubMed: 26402606]

Acuna C, Liu X, and Südhof TC (2016). How to Make an Active Zone: Unexpected Universal Functional Redundancy between RIMs and RIM-BPs. Neuron 91, 792–807. [PubMed: 27537484]

Akil O, Dyka F, Calvet C, Emptoz A, Lahlou G, Nouaille S, Boutet de Monvel J, Hardelin J-P, Hauswirth WW, Avan P, et al. (2019). Dual AAV-mediated gene therapy restores hearing in a DFNB9 mouse model. Proc. Natl. Acad. Sci. U. S. A 116, 4496–4501. [PubMed: 30782832]

Al-Moyed H, Cepeda AP, Jung S, Moser T, Kügler S, and Reisinger E (2019). A dual-AAV approach restores fast exocytosis and partially rescues auditory function in deaf otoferlin knock-out mice. EMBO Mol. Med 11, 4496–4501.

Aravamudan B, Fergestad T, Davis WS, Rodesch CK, and Broadie K (1999). Drosophila UNC-13 is essential for synaptic transmission. Nat. Neurosci 2, 965–971. [PubMed: 10526334]

Augustin I, Rosenmund C, Südhof TC, and Brose N (1999). Munc13-1 is essential for fusion competence of glutamatergic synaptic vesicles. Nature 400, 457–461. [PubMed: 10440375]

Banerjee A, Imig C, Balakrishnan K, Kershberg L, Lipstein N, Uronen R-L, Wang J, Cai X, Benseler F, Rhee JS, et al. (2021). Molecular and functional architecture of striatal dopamine release sites. Neuron 110, 248–265.e9. [PubMed: 34767769]

Basu J, Shen N, Dulubova I, Lu J, Guan R, Guryev O, Grishin NV, Rosenmund C, and Rizo J (2005). A minimal domain responsible for Munc13 activity. Nat Struct Mol Biol 12, 1017–1018. [PubMed: 16228007]

Benarroch EE (2013). Synaptic vesicle exocytosis: Molecular mechanisms and clinical implications. Neurology 80, 1981–1988. [PubMed: 23690298]

Betz A, Thakur P, Junge HJ, Ashery U, Rhee JS, Scheuss V, Rosenmund C, Rettig J, and Brose N (2001). Functional interaction of the active zone proteins Munc13-1 and RIM1 in synaptic vesicle priming. Neuron 30, 183–196. [PubMed: 11343654]

Biederer T, Kaeser PS, and Blanpied TA (2017). Transcellular Nanoalignment of Synaptic Function. Neuron 96, 680–696. [PubMed: 29096080]

Borges-Merjane C, Kim O, and Jonas P (2020). Functional Electron Microscopy, "Flash and Freeze," of Identified Cortical Synapses in Acute Brain Slices. Neuron 105, 992–1006.e6. [PubMed: 31928842]

Breustedt J, Vogt KE, Miller RJ, Nicoll RA, and Schmitz D (2003). Alpha1E-containing Ca2+ channels are involved in synaptic plasticity. Proc. Natl. Acad. Sci. U. S. A 100, 12450–12455. [PubMed: 14519849]

Brockmann MM, Maglione M, Willmes CG, Stumpf A, Bouazza BA, Velasquez LM, Grauel MK, Beed P, Lehmann M, Gimber N, et al. (2019). RIM-BP2 primes synaptic vesicles via recruitment of Munc13-1 at hippocampal mossy fiber synapses. Elife 8.

Bucan M, Abrahams BS, Wang K, Glessner JT, Herman EI, Sonnenblick LI, Alvarez Retuerto AI, Imielinski M, Hadley D, Bradfield JP, et al. (2009). Genome-wide analyses of exonic copy number variants in a family-based study point to novel autism susceptibility genes. PLoS Genet. 5, e1000536. [PubMed: 19557195]

Calakos N, Schoch S, Sudhof TC, Malenka RC, Südhof TC, Malenka RC, Sudhof TC, and Malenka RC (2004). Multiple roles for the active zone protein RIM1alpha in late stages of neurotransmitter release. Neuron 42, 889–896. [PubMed: 15207234]

Camacho M, Basu J, Trimbuch T, Chang S, Pulido-Lozano C, Chang S-S, Duluvova I, Abo-Rady M, Rizo J, and Rosenmund C (2017). Heterodimerization of Munc13 C2A domain with RIM regulates synaptic vesicle docking and priming. Nat. Commun 8, 15293. [PubMed: 28489077]

Cao YQ, Piedras-Renteria ES, Smith GB, Chen G, Harata NC, and Tsien RW (2004). Presynaptic Ca2+ channels compete for channel type-preferring slots in altered neurotransmission arising from Ca2+ channelopathy. Neuron 43, 387–400. [PubMed: 15294146]

Davydova D, Marini C, King C, Klueva J, Bischof F, Romorini S, Montenegro-Venegas C, Heine M, Schneider R, Schröder MS, et al. (2014). Bassoon specifically controls presynaptic P/Q-type Ca(2+) channels via RIM-binding protein. Neuron 82, 181–194. [PubMed: 24698275]

Deng L, Kaeser PS, Xu W, and Südhof TC (2011). RIM proteins activate vesicle priming by reversing autoinhibitory homodimerization of Munc13. Neuron 69, 317–331. [PubMed: 21262469]

Dietrich D, Kirschstein T, Kukley M, Pereverzev A, von der Brelie C, Schneider T, and Beck H (2003). Functional Specialization of Presynaptic Cav2.3 Ca2+ Channels. Neuron 39, 483–496. [PubMed: 12895422]

Dolphin AC (2012). Calcium channel auxiliary α2δ and β subunits: trafficking and one step beyond. Nat. Rev. Neurosci 13, 664–664.

Dong W, Radulovic T, Goral RO, Thomas C, Suarez Montesinos M, Guerrero-Given D, Hagiwara A, Putzke T, Hida Y, Abe M, et al. (2018). CAST/ELKS Proteins Control Voltage-Gated Ca2+ Channel Density and Synaptic Release Probability at a Mammalian Central Synapse. Cell Rep. 24, 284–293.e6. [PubMed: 29996090]

Dulubova I, Lou X, Lu J, Huryeva I, Alam A, Schneggenburger R, Sudhof TC, and Rizo J (2005). A Munc13/RIM/Rab3 tripartite complex: from priming to plasticity? EMBO J. 24, 2839–2850. [PubMed: 16052212]

Emperador-Melero J, and Kaeser PS (2020). Assembly of the presynaptic active zone. Curr. Opin. Neurobiol 63, 95–103. [PubMed: 32403081]

Emperador-Melero J, Wong MY, Wang SSH, de Nola G, Nyitrai H, Kirchhausen T, and Kaeser PS (2021). PKC-phosphorylation of Liprin-α3 triggers phase separation and controls presynaptic active zone structure. Nat. Commun 12, 3057. [PubMed: 34031393]

Fukuda M (2003). Distinct Rab binding specificity of Rim1, Rim2, rabphilin, and Noc2. Identification of a critical determinant of Rab3A/Rab27A recognition by Rim2. J. Biol. Chem 278, 15373–80. [PubMed: 12578829]

Grauel MK, Maglione M, Reddy-Alla S, Willmes CG, Brockmann MM, Trimbuch T, Rosenmund T, Pangalos M, Vardar G, Stumpf A, et al. (2016). RIM-binding protein 2 regulates release probability by fine-tuning calcium channel localization at murine hippocampal synapses. Proc. Natl. Acad. Sci 113, 11615–11620. [PubMed: 27671655]

Guzman GA, Guzman RE, Jordan N, and Hidalgo P (2019). A Tripartite Interaction Among the Calcium Channel α1- and β-Subunits and F-Actin Increases the Readily Releasable Pool of Vesicles and Its Recovery After Depletion. Front. Cell. Neurosci 13, 125. [PubMed: 31130843]

Hammarlund M, Palfreyman MT, Watanabe S, Olsen S, and Jorgensen EM (2007). Open syntaxin docks synaptic vesicles. PLoS Biol. 5, e198. [PubMed: 17645391]

Han W, Rhee J-S, Maximov A, Lao Y, Mashimo T, Rosenmund C, and Südhof TC (2004). N-glycosylation is essential for vesicular targeting of synaptotagmin 1. Neuron 41, 85–99. [PubMed: 14715137]

Han Y, Kaeser PS, Südhof TC, and Schneggenburger R (2011). RIM determines Ca^{2}+ channel density and vesicle docking at the presynaptic active zone. Neuron 69, 304–316. [PubMed: 21262468]

He E, Wierda K, van Westen R, Broeke JH, Toonen RF, Cornelisse LN, and Verhage M (2017). Munc13-1 and Munc18-1 together prevent NSF-dependent de-priming of synaptic vesicles. Nat. Commun 8, 15915. [PubMed: 28635948]

Held RG, and Kaeser PS (2018). ELKS active zone proteins as multitasking scaffolds for secretion. Open Biol. 8, 170258. [PubMed: 29491150]

Held RG, Liu C, and Kaeser PS (2016). ELKS controls the pool of readily releasable vesicles at excitatory synapses through its N-terminal coiled-coil domains. Elife 5.

Held RG, Liu C, Ma K, Ramsey AM, Tarr TB, De Nola G, Wang SSH, Wang J, van den Maagdenberg AMJM, Schneider T, et al. (2020). Synapse and Active Zone Assembly in the Absence of Presynaptic Ca2+ Channels and Ca2+ Entry. Neuron 107, 667–683.e9. [PubMed: 32616470]

Hibino H, Pironkova R, Onwumere O, Vologodskaia M, Hudspeth AJ, and Lesage F (2002). RIM binding proteins (RBPs) couple Rab3-interacting molecules (RIMs) to voltage-gated Ca(2+) channels. Neuron 34, 411–423. [PubMed: 11988172]

Hu C, Ahmed M, Melia TJ, Söllner TH, Mayer T, Rothman JE, Sollner TH, Mayer T, and Rothman JE (2003). Fusion of cells by flipped SNAREs. Science 300, 1745–1749. [PubMed: 12805548]

Hudry E, and Vandenberghe LH (2019). Therapeutic AAV Gene Transfer to the Nervous System: A Clinical Reality. Neuron 101, 839–862. [PubMed: 30844402]

Imig C, Min SW, Krinner S, Arancillo M, Rosenmund C, Südhof TC, Rhee JS, Brose N, and Cooper BH (2014). The Morphological and Molecular Nature of Synaptic Vesicle Priming at Presynaptic Active Zones. Neuron 84, 416–431. [PubMed: 25374362]

Imig C, López-Murcia FJ, Maus L, García-Plaza IH, Mortensen LS, Schwark M, Schwarze V, Angibaud J, Nägerl UV, Taschenberger H, et al. (2020). Ultrastructural Imaging of Activity-Dependent Synaptic Membrane-Trafficking Events in Cultured Brain Slices. Neuron 108, 843–860.e8. [PubMed: 32991831]

Johnson S, Halford S, Morris AG, Patel RJ, Wilkie SE, Hardcastle AJ, Moore AT, Zhang K, and Hunt DM (2003). Genomic organisation and alternative splicing of human RIM1, a gene implicated in autosomal dominant cone-rod dystrophy (CORD7). Genomics 81, 304–314. [PubMed: 12659814]

de Jong APH, Roggero CM, Ho M-R, Wong MY, Brautigam CA, Rizo J, and Kaeser PS (2018). RIM C2B Domains Target Presynaptic Active Zone Functions to PIP2-Containing Membranes. Neuron 98, 335–349.e7. [PubMed: 29606581]

Kaeser PS, and Regehr WG (2017). The readily releasable pool of synaptic vesicles. Curr. Opin. Neurobiol 43, 63–70. [PubMed: 28103533]

Kaeser PS, Kwon HB, Chiu CQ, Deng L, Castillo PE, and Sudhof TC (2008). RIM1alpha and RIM1beta are synthesized from distinct promoters of the RIM1 gene to mediate differential but overlapping synaptic functions. J. Neurosci 28, 13435–13447. [PubMed: 19074017]

Kaeser PS, Deng L, Chávez AE, Liu X, Castillo PE, and Südhof TC (2009). ELKS2alpha/CAST deletion selectively increases neurotransmitter release at inhibitory synapses. Neuron 64, 227–239. [PubMed: 19874790]

Kaeser PS, Deng L, Wang Y, Dulubova I, Liu X, Rizo J, and Südhof TC (2011). RIM proteins tether Ca2+ channels to presynaptic active zones via a direct PDZ-domain interaction. Cell 144, 282–295. [PubMed: 21241895]

Kanaji S, Iwahashi J, Kida Y, Sakaguchi M, and Mihara K (2000). Characterization of the signal that directs Tom20 to the mitochondrial outer membrane. J. Cell Biol 151, 277–288. [PubMed: 11038175]

Kawabe H, Mitkovski M, Kaeser PS, Hirrlinger J, Opazo F, Nestvogel D, Kalla S, Fejtova A, Verrier SESE, Bungers SRSR, et al. (2017). ELKS1 localizes the synaptic vesicle priming protein bMunc13-2 to a specific subset of active zones. J. Cell Biol 216, 1143–1161. [PubMed: 28264913]

Kittel RJ, Wichmann C, Rasse TM, Fouquet W, Schmidt M, Schmid A, Wagh DA, Pawlu C, Kellner RR, Willig KI, et al. (2006). Bruchpilot promotes active zone assembly, Ca2+ channel clustering, and vesicle release. Science 312, 1051–1054. [PubMed: 16614170]

Koushika SP, Richmond JE, Hadwiger G, Weimer RM, Jorgensen EM, and Nonet ML (2001). A post-docking role for active zone protein Rim. Nat. Neurosci 4, 997–1005. [PubMed: 11559854]

Krumm N, Turner TN, Baker C, Vives L, Mohajeri K, Witherspoon K, Raja A, Coe BP, Stessman HA, He Z-X, et al. (2015). Excess of rare, inherited truncating mutations in autism. Nat. Genet 47, 582–588. [PubMed: 25961944]

Kushibiki Y, Suzuki T, Jin Y, and Taru H (2019). RIMB-1/RIM-Binding Protein and UNC-10/RIM Redundantly Regulate Presynaptic Localization of the Voltage-Gated Calcium Channel in Caenorhabditis elegans. J. Neurosci 39, 8617–8631. [PubMed: 31530643]

Lin Y, McDonough SI, and Lipscombe D (2004). Alternative Splicing in the Voltage-Sensing Region of N-Type CaV2.2 Channels Modulates Channel Kinetics. J. Neurophysiol 92, 2820–2830. [PubMed: 15201306]

Lipstein N, Sakaba T, Cooper BH, Lin K-H, Strenzke N, Ashery U, Rhee J-S, Taschenberger H, Neher E, and Brose N (2013). Dynamic control of synaptic vesicle replenishment and short-term plasticity by Ca(2+)-calmodulin-Munc13-1 signaling. Neuron 79, 82–96. [PubMed: 23770256]

Liu C, Bickford LS, Held RG, Nyitrai H, Südhof TC, and Kaeser PS (2014). The active zone protein family ELKS supports Ca2+ influx at nerve terminals of inhibitory hippocampal neurons. J. Neurosci 34, 12289–12303. [PubMed: 25209271]

Liu C, Kershberg L, Wang J, Schneeberger S, and Kaeser PS (2018). Dopamine Secretion Is Mediated by Sparse Active Zone-like Release Sites. Cell 172, 706–718.e15. [PubMed: 29398114]

Liu KSY, Siebert M, Mertel S, Knoche E, Wegener S, Wichmann C, Matkovic T, Muhammad K, Depner H, Mettke C, et al. (2011). RIM-binding protein, a central part of the active zone, is essential for neurotransmitter release. Science 334, 1565–1569. [PubMed: 22174254]

Ma C, Su L, Seven AB, Xu Y, and Rizo J (2013). Reconstitution of the Vital Functions of Munc18 and Munc13 in Neurotransmitter Release. Science 339, 421–425. [PubMed: 23258414]

Matkovic T, Siebert M, Knoche E, Depner H, Mertel S, Owald D, Schmidt M, Thomas U, Sickmann A, Kamin D, et al. (2013). The Bruchpilot cytomatrix determines the size of the readily releasable pool of synaptic vesicles. J. Cell Biol 202, 667–683. [PubMed: 23960145]

McDonald NA, Fetter RD, and Shen K (2020). Assembly of synaptic active zones requires phase separation of scaffold molecules. Nature 588, 454–458. [PubMed: 33208945]

Myoga MH, and Regehr WG (2011). Calcium Microdomains Near R-Type Calcium Channels Control the Induction of Presynaptic Long-Term Potentiation at Parallel Fiber to Purkinje Cell Synapses. J. Neurosci 31, 5235–5243. [PubMed: 21471358]

Nyitrai H, Wang SSH, and Kaeser PS (2020). ELKS1 Captures Rab6-Marked Vesicular Cargo in Presynaptic Nerve Terminals. Cell Rep. 31, 107712. [PubMed: 32521280]

O'Roak BJ, Vives L, Girirajan S, Karakoc E, Krumm N, Coe BP, Levy R, Ko A, Lee C, Smith JD, et al. (2012). Sporadic autism exomes reveal a highly interconnected protein network of de novo mutations. Nature 485, 246–250. [PubMed: 22495309]

Oh KH, Krout MD, Richmond JE, and Kim H (2021). UNC-2 CaV2 Channel Localization at Presynaptic Active Zones Depends on UNC-10/RIM and SYD-2/Liprin-α in Caenorhabditis elegans. J. Neurosci 41, 4782–4794. [PubMed: 33975919]

Page KM, Rothwell SW, and Dolphin AC (2016). The CaVβ Subunit Protects the I-II Loop of the Voltage-gated Calcium Channel CaV2.2 from Proteasomal Degradation but Not Oligoubiquitination. J. Biol. Chem 291, 20402–20416. [PubMed: 27489103]

Parthier D, Kuner T, and Körber C (2018). The presynaptic scaffolding protein Piccolo organizes the readily releasable pool at the calyx of Held. J. Physiol 596, 1485–1499. [PubMed: 29194628]

Pereverzev A, Mikhna M, Vajna R, Gissel C, Henry M, Weiergräber M, Hescheler J, Smyth N, and Schneider T (2002). Disturbances in Glucose-Tolerance, Insulin-Release, and Stress-Induced Hyperglycemia upon Disruption of the Cav2.3 (α1E) Subunit of Voltage-Gated Ca2+ Channels. Mol. Endocrinol 16, 884–895. [PubMed: 11923483]

Quade B, Camacho M, Zhao X, Orlando M, Trimbuch T, Xu J, Li W, Nicastro D, Rosenmund C, and Rizo J (2019). Membrane bridging by Munc13-1 is crucial for neurotransmitter release. Elife 8.

Rebola N, Reva M, Kirizs T, Szoboszlay M, Lőrincz A, Moneron G, Nusser Z, and DiGregorio DA (2019). Distinct Nanoscale Calcium Channel and Synaptic Vesicle Topographies Contribute to the Diversity of Synaptic Function. Neuron 104, 693–710.e9. [PubMed: 31558350]

Reddy-Alla S, Bohme MA, Reynolds E, Beis C, Grasskamp AT, Mampell MM, Maglione M, Jusyte M, Rey U, Babikir H, et al. (2017). Stable Positioning of Unc13 Restricts Synaptic Vesicle Fusion to Defined Release Sites to Promote Synchronous Neurotransmission. Neuron 95, 1350–1364.e12. [PubMed: 28867551]

Richmond JE, Davis WS, and Jorgensen EM (1999). UNC-13 is required for synaptic vesicle fusion in C. elegans. Nat. Neurosci 2, 959–964. [PubMed: 10526333]

Rosenmund C, and Stevens CF (1996). Definition of the readily releasable pool of vesicles at hippocampal synapses. Neuron 16, 1197–1207. [PubMed: 8663996]

Sakamoto H, Ariyoshi T, Kimpara N, Sugao K, Taiko I, Takikawa K, Asanuma D, Namiki S, and Hirose K (2018). Synaptic weight set by Munc13-1 supramolecular assemblies. Nat. Neurosci 21, 41–49. [PubMed: 29230050]

Schikorski T, and Stevens CF (2001). Morphological correlates of functionally defined synaptic vesicle populations. Nat. Neurosci 4, 391–395. [PubMed: 11276229]

Schneider R, Hosy E, Kohl J, Klueva J, Choquet D, Thomas U, Voigt A, and Heine M (2015). Mobility of Calcium Channels in the Presynaptic Membrane. Neuron 86, 672–679. [PubMed: 25892305]

Schoch S, Deák F, Königstorfer a, Mozhayeva M, Sara Y, Südhof TC, Kavalali ET, Deak F, Konigstorfer A, Mozhayeva M, et al. (2001). SNARE function analyzed in synaptobrevin/VAMP knockout mice. Science 294, 1117–1122. [PubMed: 11691998]

Schoch S, Castillo PE, Jo T, Mukherjee K, Geppert M, Wang Y, Schmitz F, Malenka RC, and Südhof TC (2002). RIM1alpha forms a protein scaffold for regulating neurotransmitter release at the active zone. Nature 415, 321–326. [PubMed: 11797009]

Siksou L, Varoqueaux F, Pascual O, Triller A, Brose N, and Marty S (2009). A common molecular basis for membrane docking and functional priming of synaptic vesicles. Eur. J. Neurosci 30, 49–56. [PubMed: 19558619]

Spangler SA, Schmitz SK, Kevenaar JT, de Graaff E, de Wit H, Demmers J, Toonen RF, and Hoogenraad CC (2013). Liprin-alpha2 promotes the presynaptic recruitment and turnover of RIM1/CASK to facilitate synaptic transmission. J. Cell Biol 201, 915–928. [PubMed: 23751498]

Sternberg SR (1983). Biomedical Image Processing. Computer (Long. Beach. Calif). 16, 22–34.

Sudhof TC (2004). The synaptic vesicle cycle. Annu. Rev. Neurosci 27, 509–547. [PubMed: 15217342]

Südhof TC (2012). The Presynaptic Active Zone. Neuron 75, 11–25. [PubMed: 22794257]

Sun J, and Roy S (2021). Gene-based therapies for neurodegenerative diseases. Nat. Neurosci

Tang A-H, Chen H, Li TP, Metzbower SR, MacGillavry HD, and Blanpied TA (2016). A trans-synaptic nanocolumn aligns neurotransmitter release to receptors. Nature 536, 210–214. [PubMed: 27462810]

Thevenon J, Callier P, Andrieux J, Delobel B, David A, Sukno S, Minot D, Mosca Anne L, Marle N, Sanlaville D, et al. (2013). 12p13.33 microdeletion including ELKS/ERC1, a new locus associated with childhood apraxia of speech. Eur. J. Hum. Genet 21, 82–88. [PubMed: 22713806]

Todorov B, van de Ven RCG, Kaja S, Broos LAM, Verbeek SJ, Plomp JJ, Ferrari MD, Frants RR, and van den Maagdenberg AMJM (2006). Conditional inactivation of the Cacna1a gene in transgenic mice. Genesis 44, 589–594. [PubMed: 17146767]

Tucker WC, Weber T, and Chapman ER (2004). Reconstitution of Ca2+-regulated membrane fusion by synaptotagmin and SNAREs. Science 304, 435–438. [PubMed: 15044754]

Varoqueaux F, Sigler A, Rhee JS, Brose N, Enk C, Reim K, and Rosenmund C (2002). Total arrest of spontaneous and evoked synaptic transmission but normal synaptogenesis in the absence of Munc13-mediated vesicle priming. Proc. Natl. Acad. Sci. U. S. A 99, 9037–9042. [PubMed: 12070347]

Verhage M, and Sørensen JB (2020). SNAREopathies: Diversity in Mechanisms and Symptoms. Neuron.

Wang SSH, Held RG, Wong MY, Liu C, Karakhanyan A, and Kaeser PS (2016). Fusion Competent Synaptic Vesicles Persist upon Active Zone Disruption and Loss of Vesicle Docking. Neuron 91, 777–791. [PubMed: 27537483]

Wang Y, Okamoto M, Schmitz F, Hofmann K, and Sudhof TC (1997). Rim is a putative Rab3 effector in regulating synaptic-vesicle fusion. Nature 388, 593–598. [PubMed: 9252191]

Wong MY, Liu C, Wang SSH, Roquas ACF, Fowler SC, and Kaeser PS (2018). Liprin-α3 controls vesicle docking and exocytosis at the active zone of hippocampal synapses. Proc. Natl. Acad. Sci. U. S. A 115, 2234–2239. [PubMed: 29439199]

Wu LG, Westenbroek RE, Borst JG, Catterall WA, and Sakmann B (1999). Calcium channel types with distinct presynaptic localization couple differentially to transmitter release in single calyx-type synapses. J. Neurosci 19, 726–736. [PubMed: 9880593]

Wu X, Cai Q, Shen Z, Chen X, Zeng M, Du S, and Zhang M (2019). RIM and RIM-BP Form Presynaptic Active-Zone-like Condensates via Phase Separation. Mol. Cell 73, 971–984.e5. [PubMed: 30661983]

Wu X, Ganzella M, Zhou J, Zhu S, Jahn R, and Zhang M (2021). Vesicle Tethering on the Surface of Phase-Separated Active Zone Condensates. Mol. Cell 81, 13–24.e7. [PubMed: 33202250]

Wu Z, Yang H, and Colosi P (2010). Effect of genome size on AAV vector packaging. Mol. Ther 18, 80–86. [PubMed: 19904234]

Zarebidaki F, Camacho M, Brockmann MM, Trimbuch T, Herman MA, and Rosenmund C (2020). Disentangling the Roles of RIM and Munc13 in Synaptic Vesicle Localization and Neurotransmission. J. Neurosci 40, 9372–9385. [PubMed: 33139401]

Zhen M, and Jin Y (1999). The liprin protein SYD-2 regulates the differentiation of presynaptic termini in C. elegans. Nature 401, 371–375. [PubMed: 10517634]

Zucker RS, and Regehr WG (2002). Short-term synaptic plasticity. Annu. Rev. Physiol 64, 355–405. [PubMed: 11826273]

Highlights

- RIM+ELKS knockout disrupts active zones and vesicle docking, priming and release
- RIM zinc fingers rescue fusion-competence by recruiting Munc13 to undocked vesicles
- Linking RIM zinc fingers to $Ca_V\beta4$ restores docking and Ca^{2+}-triggering of release
- This 80 kDa β4-Zn protein bypasses the need for megadalton-sized secretory machines

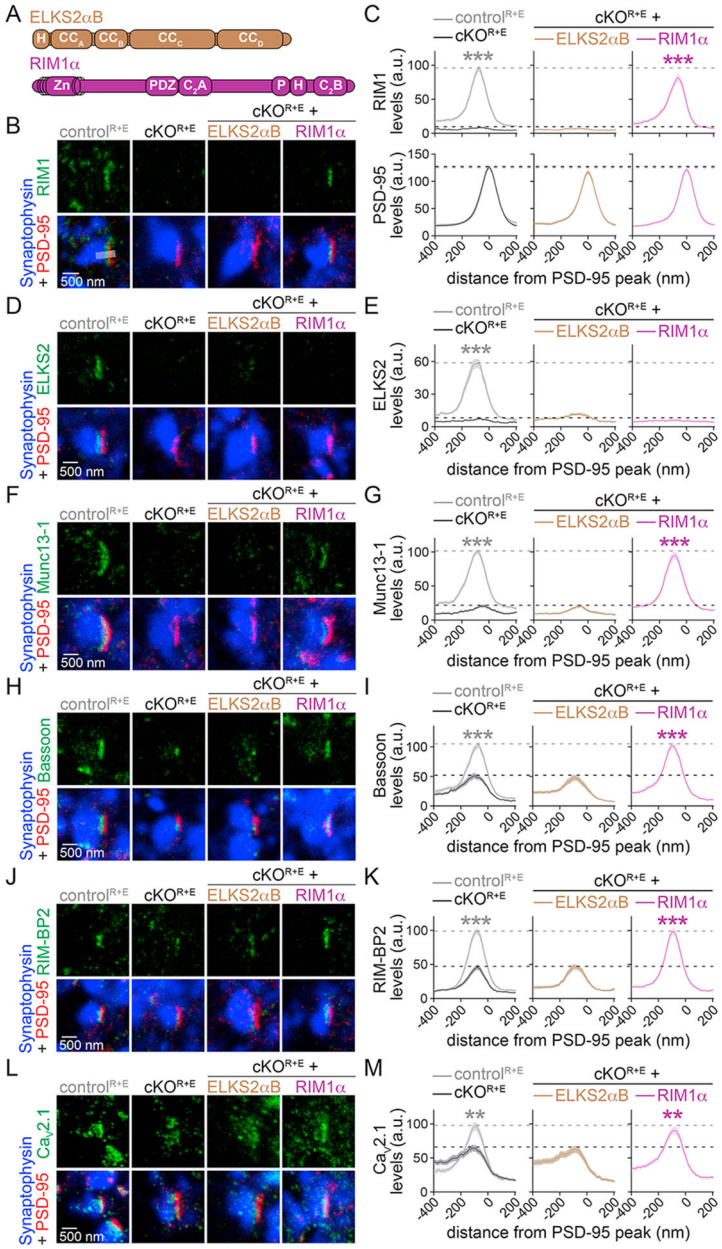

Figure 1. RIM re-expression restores active zone structure in RIM and ELKS knockout neurons

(**A**) Schematic of HA-tagged ELKS2αB and RIM1α, H: HA tag, CC: coiled-coil region, Zn: zinc finger domain, PDZ: PDZ domain, C_2A and C_2B: C_2 domains, P: proline rich (PxxP-) motif.

(**B, C**) Sample STED images (B) and quantification (C) of side-view synapses of cultured hippocampal neurons after knockout of RIM and ELKS (cKO^{R+E}; through expression of cre-lentiviruses in neurons of floxed mice) or in corresponding control neurons ($control^{R+E}$; expression of recombination-deficient cre in the same neurons), and in cKO^{R+E} neurons after lentiviral re-expression of ELKS2αB or RIM1α. Neurons were antibody-stained for RIM1 (imaged in STED), PSD-95 (imaged in STED), and Synaptophysin (imaged in confocal). Peak position and levels (C) were analyzed in line profiles (600 nm x 200

nm, grey shaded area in B, for STED analysis workflow, see Figs. S1A-S1D) positioned perpendicular to the center of elongated PSD-95 structure and aligned to the PSD-95 peak, dotted lines mark control^{R+E} (grey) and cKO^{R+E} (black) levels for comparison, a.u.: arbitrary units, 60 synapses/3 cultures each.

(**D**-**M**) Same as (B, C), but for ELKS2 (D, E), Munc13-1 (F, G), Bassoon (H, I), RIM-BP2 (J, K) or $Ca_V2.1$ (L, M), 60/3 each. PSD-95 levels were assessed as in C and were similar in each condition.

Data are mean ± SEM; $^{**}P < 0.01$, $^{***}P < 0.001$ compared to cKO^{R+E} as determined by two-way ANOVA followed by Dunnett's multiple comparisons post-hoc tests. For STED workflow, evaluation of Liprin-α3 by STED, and assessment of rescue protein expression by Western blotting, see Fig. S1; for additional confocal and STED experiments, see Fig. S2.

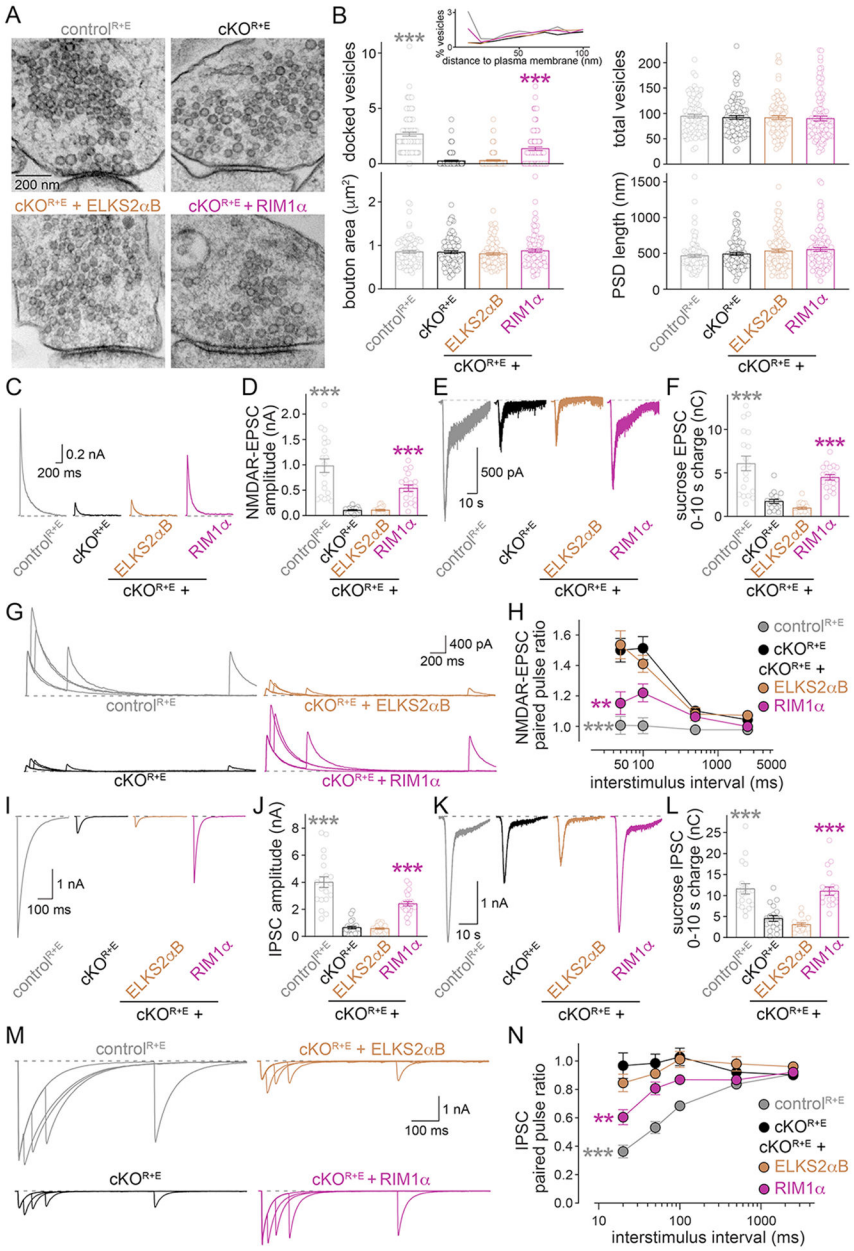

Figure 2. RIM restores active zone functions in neurons with disrupted active zones

(**A, B**) Sample images (A) and analyses (B) of synapses of high-pressure frozen neurons analyzed by electron microscopy. In B, the number of docked vesicles per synapse profile is provided, and the inset shows vesicle distribution within 100 nm from the presynaptic plasma membrane in 10 nm bins. Quantification was performed on single sections, control^{R+E} 96 synapses/2 cultures, cKO^{R+E} 100/2, cKO^{R+E} + ELKS2αB 100/2, and cKO^{R+E} + RIM1α 98/2.

(**C, D**) Sample traces (C) and quantification (D) of EPSCs evoked by focal electrical stimulation and monitored via NMDARs, control^{R+E} 19 cells/3 cultures, cKO^{R+E} 18/3, cKO^{R+E} + ELKS2αB, 18/3, and cKO^{R+E} + RIM1α 19/3.

(**E, F**) Sample traces (E) and quantification (F) of EPSCs triggered by hypertonic sucrose and monitored via AMPARs, the first 10 s were quantified to estimate the RRP, 19/3 each.
(**G, H**) Sample traces (G) and quantification (H) of EPSC paired pulse ratios monitored via NMDARs to estimate p, 16/3 each.
(**I-N**) As C-H, but for electrically evoked IPSCs (I, J), sucrose-evoked IPSCs (K, L) and IPSC paired pulse ratios (M, N), J: control^{R+E} 20/3, cKO^{R+E} 21/3, cKO^{R+E} + ELKS2αB 21/3, and cKO^{R+E} + RIM1α 22/3; L: 19/3 each; N: 15/3 each.
Data are mean ± SEM; $^{**}P < 0.01$, $^{***}P < 0.001$ compared to cKO^{R+E} as determined by Brown-Forsythe ANOVA followed by Games-Howell's multiple comparisons post-hoc test (B, docked vesicles), Brown-Forsythe ANOVA followed by Dunnett's T3 multiple comparisons post-hoc test (D), Kruskal-Wallis tests followed by Dunn's multiple comparisons post-hoc tests (F, J and L), or by two-way ANOVA followed by Dunnett's multiple comparisons post-hoc tests (H and N). For analyses of NMDAR-EPSCs in low extracellular Ca^{2+} or with competitive NMDAR antagonists, see Fig. S3.

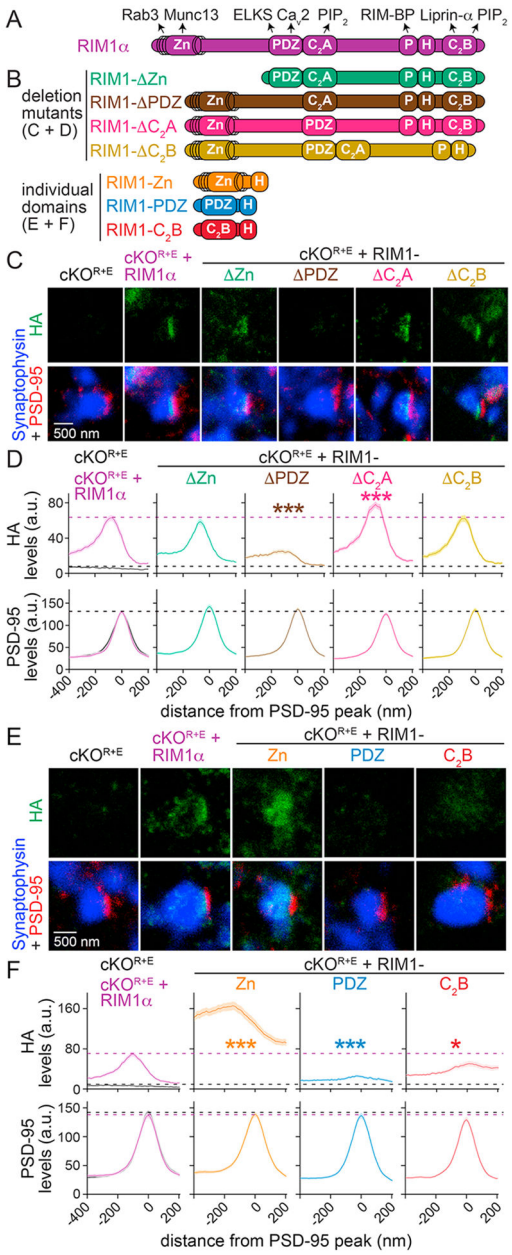

Figure 3. RIM PDZ domains mediate RIM active zone localization while zinc fingers associate with synaptic vesicles

(**A**) Schematic of RIM1α and of select presynaptic interactors.

(**B**) Schematic of RIM1 deletion mutants and individual domains used in C-F.

(**C, D**) Sample STED images (C) and quantification (D) of side-view synapses stained for HA (STED), PSD-95 (STED), and Synaptophysin (confocal), dotted lines mark cKO^{R+E} (black) and cKO^{R+E} + RIM1α (purple) levels for comparison, 60 synapses/3 cultures each.

(**E, F**) Same as (C, D), but for individual domains, 60/3 each.

Data are mean ± SEM; $*P < 0.05$, $***P < 0.001$ compared to cKO^{R+E} + RIM1α as determined by two-way ANOVA followed by Dunnett's tests. For rescue expression analyses, see Figs. S4A and S4B.

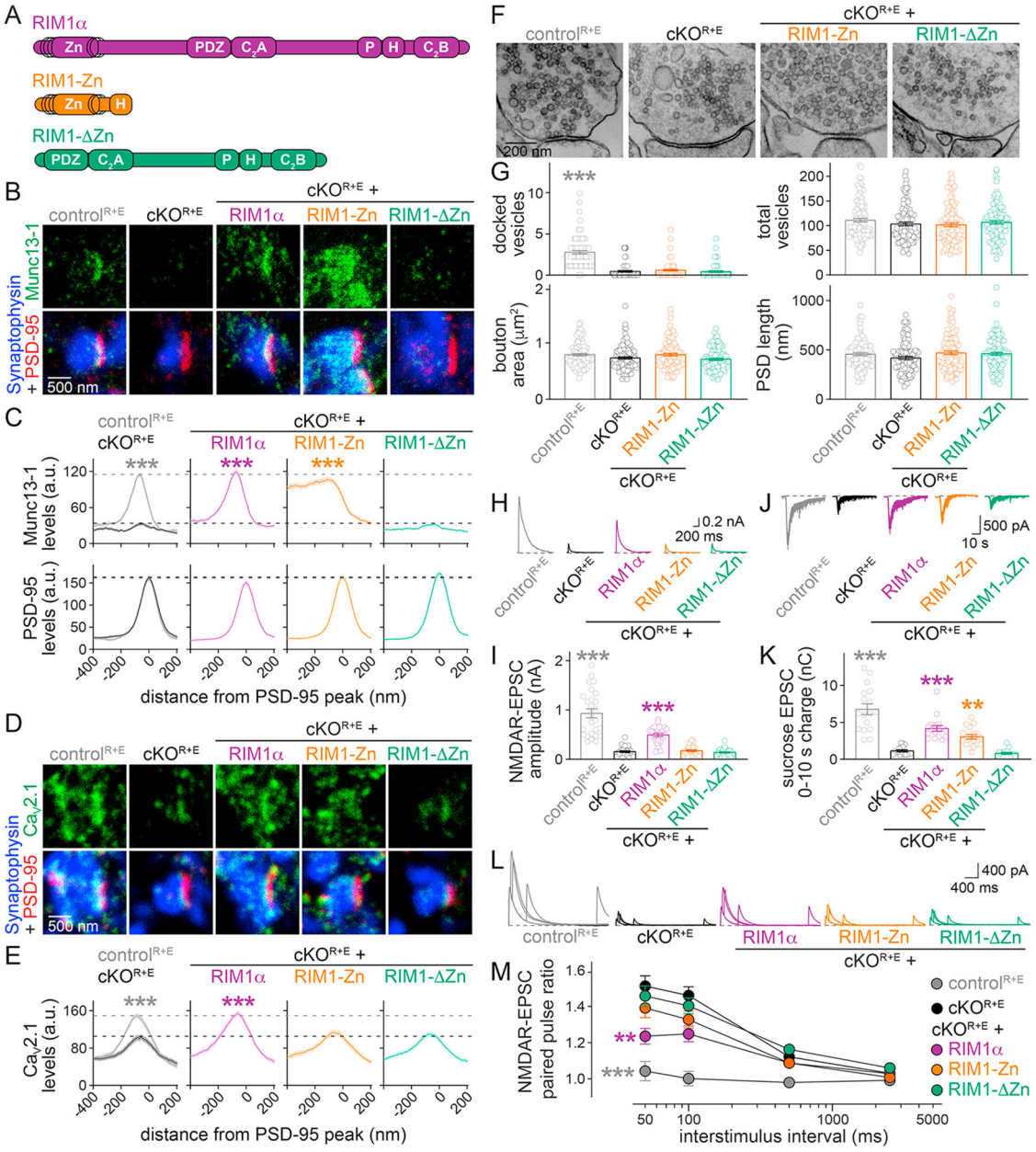

Figure 4. RIM zinc finger re-expression enhances fusogenicity of undocked vesicles through Munc13 recruitment

(**A**) Schematic of rescue proteins.

(**B, C**) Sample STED images (B) and quantification (C) of side-view synapses stained for Munc13-1 (STED), PSD-95 (STED), and Synaptophysin (confocal), dotted lines mark control^{R+E} (grey) and cKO^{R+E} (black) levels for comparison, 60 synapses/3 cultures each.

(**D, E**) Same as (B, C), but for $Ca_V2.1$, 60/3 each. PSD-95 levels were similar across conditions, but are not shown for simplicity.

(**F, G**) Sample electron microscopic images (F) and analyses (G) of synapses of high-pressure frozen neurons, control^{R+E} 105 synapses/2 cultures, cKO^{R+E} 110/2, cKO^{R+E} + RIM1-Zn 105/2, and cKO^{R+E} + RIM1-ΔZn 102/2.

(**H, I**) Sample traces (H) and quantification (I) of EPSCs evoked by focal electrical stimulation, 26 cells/4 cultures each.
(**J, K**) Sample traces (J) and quantification (K) of EPSCs triggered by hypertonic sucrose, 17/3 each.
(**L, M**) Sample traces (L) and quantification (M) of paired pulse ratios, 25/4 each.
Data are mean ± SEM; $^{**}P < 0.01$, $^{***}P < 0.001$ compared to cKO^{R+E} as determined by two-way ANOVA followed by Dunnett's tests (C, E and M), Brown-Forsythe ANOVA followed by Games-Howell's multiple comparisons post-hoc test (G, docked vesicles), or by Kruskal-Wallis tests followed by Dunn's multiple comparisons post-hoc tests (I and K). For recordings of IPSCs, see Figs. S4C-S4H.

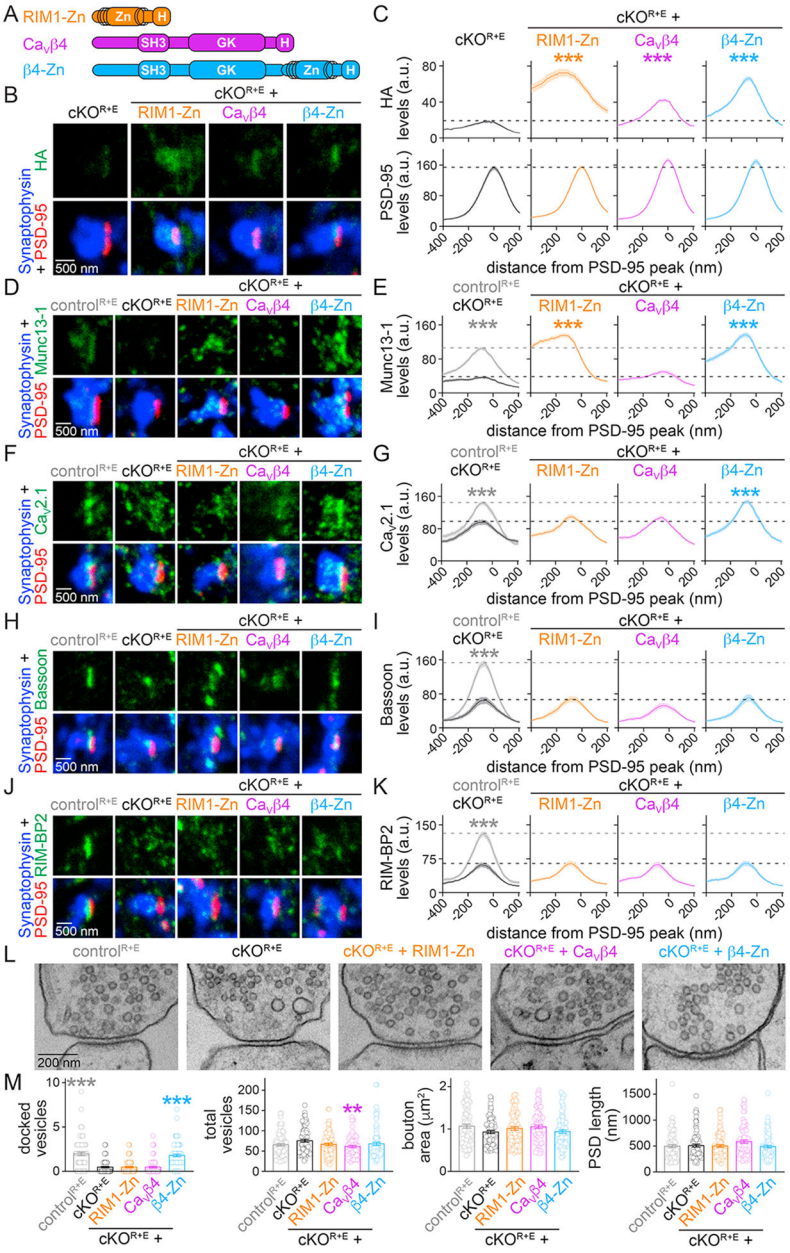

Figure 5. A $Ca_V\beta4$-RIM zinc finger fusion-protein recruits priming machinery close to Ca^{2+} channels and reconstitutes vesicle docking

(**A**) Schematic of rescue proteins. SH3, src homology domain 3; GK, guanylate kinase domain.

(**B, C**) Sample STED images (B) and quantification (C) of side-view synapses stained for HA (STED), PSD-95 (STED), and Synaptophysin (confocal), dotted lines mark cKO^{R+E} (black) levels for comparison, 60 synapses/3 cultures each.

(**D-K**) Same as (B, C), but for Munc13-1 (D, E), $Ca_V2.1$ (F, G), Bassoon (H, I), and RIM-BP2 (J, K), 60/3 each. PSD-95 levels were similar across conditions, but are not shown for simplicity, dotted lines mark $control^{R+E}$ (grey) and cKO^{R+E} (black) levels for comparison.

(**L, M**) Sample electron microscopic images **(L)** and analyses (M) of synapses of high-pressure frozen neurons, control^{R+E} 83 synapses/2 cultures, cKO^{R+E} 85/2, cKO^{R+E} + RIM1-Zn 84/2, cKO^{R+E} + $Ca_V\beta4$ 83/2, and cKO^{R+E} + β4-Zn 87/2.

Data are mean ± SEM; $^{**}P < 0.01$, $^{***}P < 0.001$ compared to cKO^{R+E} as determined by two-way ANOVA followed by Dunnett's tests (C, E, G, I and K), Brown-Forsythe ANOVA followed by Games-Howell's multiple comparisons post-hoc test (M, docked vesicles), or by one-way ANOVA followed by Dunnett's multiple comparisons post-hoc tests (M, total vesicles). For assessment of various rescue fusion-proteins, STED analyses of Cavβ4, and expression level analyses of rescue proteins, see Fig. S5.

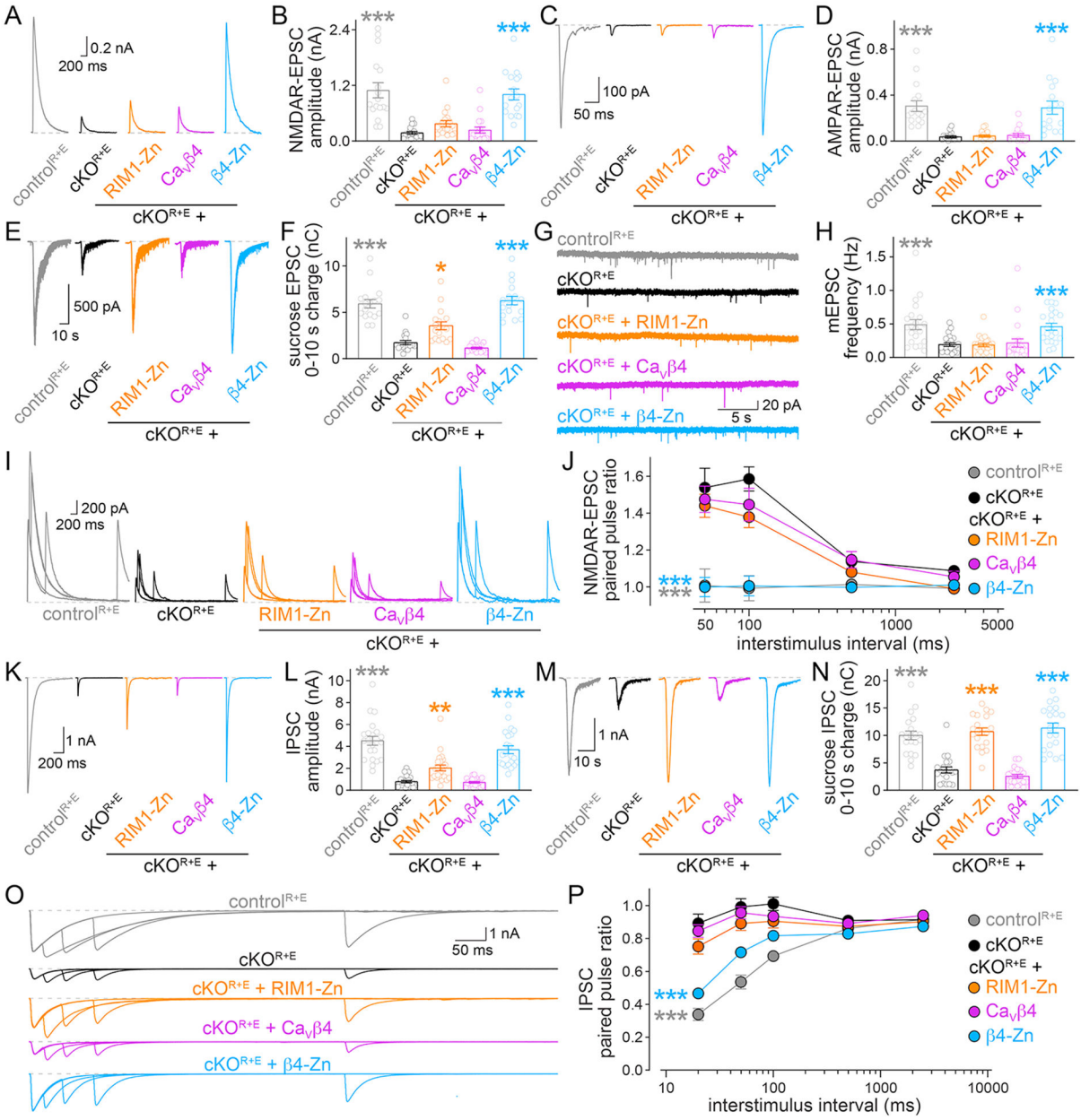

Figure 6. β4-Zn reconstitutes vesicle release in neurons with disrupted active zones

(**A-D**) Sample traces (A, C) and quantification (B, D) of EPSCs (A, B: NMDAR, C, D: AMPAR) evoked by focal electrical stimulation, B: control^{R+E} 17 cells/3 cultures, cKO^{R+E} 17/3, cKO^{R+E} + RIM1-Zn 18/3, cKO^{R+E} + Ca_Vβ4 18/3, and cKO^{R+E} + β4-Zn 17/3, D: 16/3 each.

(**E, F**) Sample traces (E) and quantification (F) of EPSCs triggered by hypertonic sucrose, 17/3 each.

(**G, H**) Sample traces (G) and quantification of mEPSC frequencies (H), control^{R+E} 21/3, cKO^{R+E} 23/3, cKO^{R+E} + RIM1-Zn 23/3, cKO^{R+E} + Ca_Vβ4 22/3, and cKO^{R+E} + β4-Zn 21/3.

(**I, J**) Sample traces (I) and quantification (J) of EPSC paired pulse ratios, control^{R+E} 16/3, cKO^{R+E} 16/3, cKO^{R+E} + RIM1-Zn 17/3, cKO^{R+E} + Ca_Vβ4 16/3, and cKO^{R+E} + β4-Zn 17/3.

(**K**-**P**) As A-F and I, J, but for electrically evoked IPSCs (K, L), sucrose-evoked IPSCs (M, N) and IPSC paired pulse ratios (O, P), L: control^{R+E} 21/4, cKO^{R+E} 21/4, cKO^{R+E} + RIM1-Zn 24/4, cKO^{R+E} + $Ca_V\beta4$ 22/4, and cKO^{R+E} + β4-Zn 22/4; N: 20/3 each; P: control^{R+E} 20/4, cKO^{R+E} 19/4, cKO^{R+E} + RIM1-Zn 20/4, cKO^{R+E} + $Ca_V\beta4$ 19/4, and cKO^{R+E} + β4-Zn 20/4.

Data are mean ± SEM; *$P < 0.05$, **$P < 0.01$, ***$P < 0.001$ compared to cKO^{R+E} as determined by Kruskal-Wallis tests followed by Dunn's multiple comparisons post-hoc tests (B, D, F, H, L and N) or by two-way ANOVA followed by Dunnett's tests (J and P). For assessment of mEPSC amplitudes and kinetics, and Ca^{2+}-, EGTA- and sucrose concentration-dependence of release, see Fig. S6.

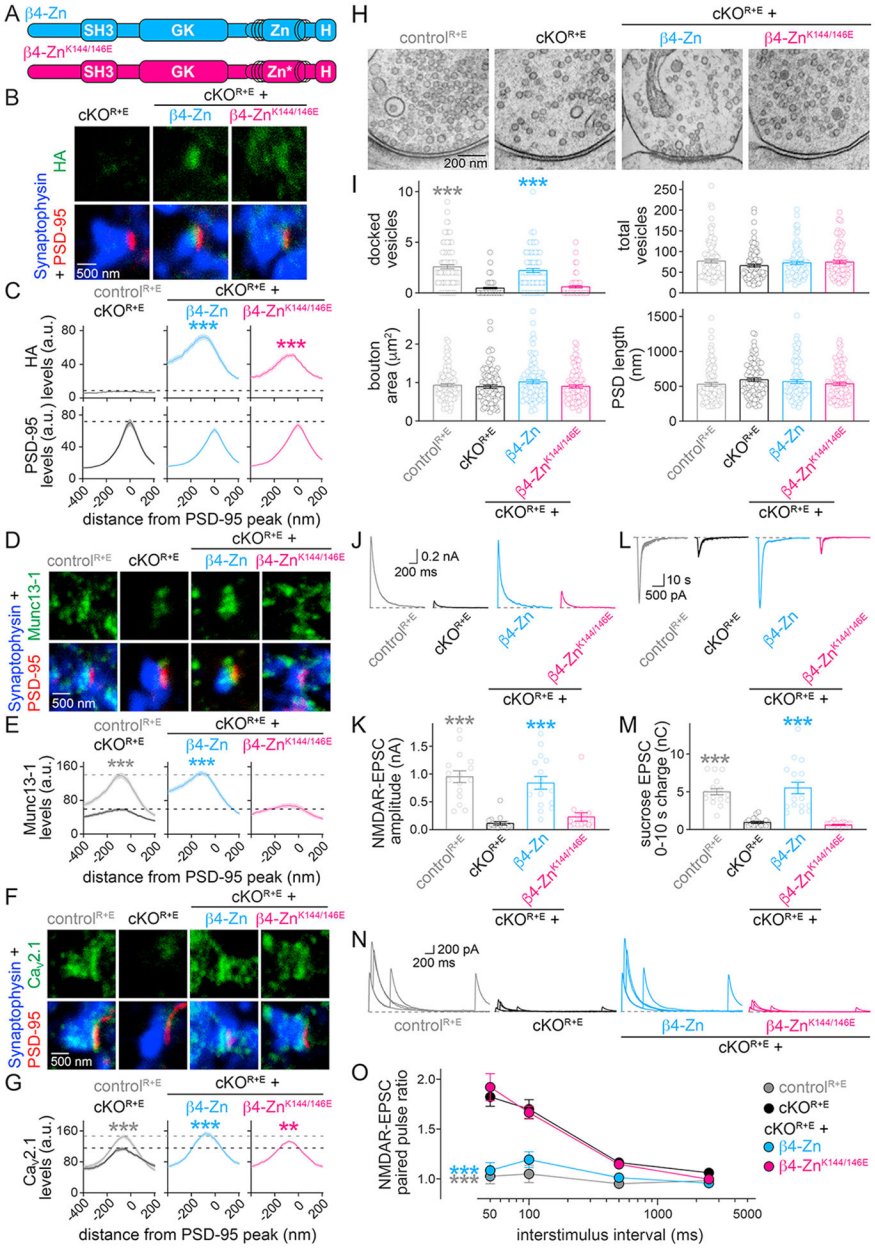

Figure 7. Binding of β4-Zn to Munc13 mediates Munc13 recruitment, vesicle docking and release

(**A**) Schematic of rescue proteins.

(**B, C**) Sample STED images (C) and quantification (D) of side-view synapses stained for HA (STED), PSD-95 (STED), and Synaptophysin (confocal), dotted lines mark cKO^{R+E} levels for comparison, 60 synapses/3 cultures each.

(**D-G**) Same as (B, C), but for Munc13-1 (D, E) and $Ca_V2.1$ (F, G), 60/3 each. PSD-95 levels were similar across conditions, but are not shown for simplicity, dotted lines mark control^{R+E} (grey) and cKO^{R+E} (black) levels for comparison.

(**H, I**) Sample electron microscopic images (H) and analyses (I) of synapses of high-pressure frozen neurons, control^{R+E} 100 synapses/2 cultures, cKO^{R+E} 99/2, cKO^{R+E} + β4-Zn 99/2, and cKO^{R+E} + β4-Zn$^{K144/146E}$ 99/2.

(**J, K**) Sample traces (J) and quantification (K) of EPSCs evoked by focal electrical stimulation, 16 cells/4 cultures each.

(**L, M**) Sample traces (L) and quantification (M) of EPSCs triggered by hypertonic sucrose, 17/3 each.

(**N, O**) Sample traces (N) and quantification (O) of EPSC paired pulse ratios, 16/4 each. Data are mean ± SEM; $^{**}P < 0.01$, $^{***}P < 0.001$ compared to cKO^{R+E} as determined by two-way ANOVA followed by Dunnett's tests (C, E, G and O), Brown-Forsythe ANOVA followed by Games-Howell's multiple comparisons post-hoc test (I, docked vesicles), or by Kruskal-Wallis tests followed by Dunn's multiple comparisons posthoc tests (K and M). For assessment of rescue protein expression, and for recordings of IPSCs with β4-$Zn^{K144/146E}$ expression, see Fig. S7.

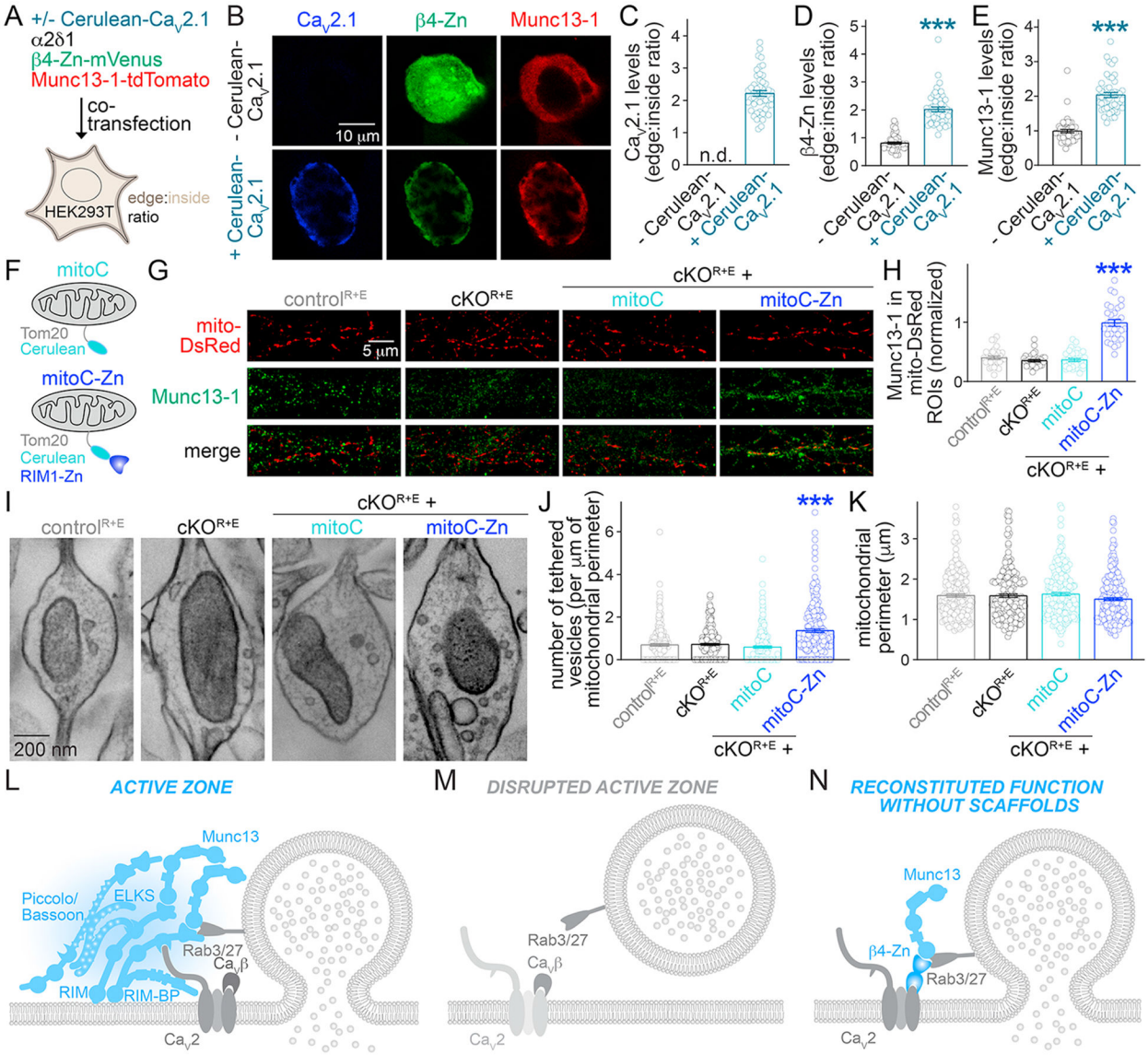

Figure 8. Redirecting the docking complex to other membranes and working model

(**A**) Schematic of experiments in transfected HEK293T cells.

(**B-E**) Sample confocal images (B) and quantification of edge:inside ratio for $Ca_V2.1$ (C), β4-Zn (D) and Munc13-1 (E), 48 cells/3 transfections each.

(**F**) Schematic of targeting of RIM1-Zn to mitochondria in neurons.

(**G, H**) Representative confocal images (G) and quantification of Munc13-1 levels (H) in mitochondrial ROIs in control^{R+E} and cKO^{R+E} neurons, and in cKO^{R+E} neurons transduced with lentiviruses expressing mitoC or mitoC-Zn (and mito-DsRed in all conditions), 30 images/3 cultures each.

(**I-K**) Sample electron microscopic images (I) and quantification (J, K) of vesicles tethered to the surface of axonal mitochondria, control^{R+E} 221 mitochondria/2 cultures, cKO^{R+E} 218/2, cKO^{R+E} + mitoC 218/2, and cKO^{R+E} + mitoC-Zn 215/2.

(**L-N**) Working model of the presynaptic active zone (L, adapted from previous models (Biederer et al., 2017; de Jong et al., 2018; Kaeser et al., 2011)). RIM+ELKS knockout leads

to loss of many active zone scaffolds and to impaired vesicle docking, priming and release (M). Reconstitution of synaptic function is mediated by a β4-Zn fusion protein that docks primed vesicles close to Ca^{2+} channels in the absence of most active zone scaffolds (N). Data are mean ± SEM; ***$P < 0.001$ as determined by Welch's t test (D and E, compared to - Cerulean-$Ca_V2.1$) or by Brown-Forsythe ANOVA followed by Dunnett's T3 multiple comparisons post-hoc test (H, compared to cKO^{R+E}), and by Brown-Forsythe ANOVA followed by Games-Howell's multiple comparisons post-hoc test (J, compared to cKO^{R+E}). For protein expression analyses, assessment of mitoC-Zn localization by confocal microscopy, and additional analyses of electron microscopic images, see Fig. S8.

Key Resources Table

REAGENT or RESOURCE	SOURCE	IDENTIFIER
Antibodies		
guinea pig anti-Bassoon (lab antibody code (LAC): A67)	Synaptic Systems	Cat#: 141 004; RRID: AB_2290619
mouse anti-β-actin (LAC: A127)	Sigma-Aldrich	Cat#: A1978; RRID: AB_476692
rabbit anti-$Ca_V2.1$ (LAC: A46)	Synaptic Systems	Cat#: 152 203; RRID: AB_2619841
mouse anti-$Ca_V\beta4$ (LAC: A123)	UC Davis/NIH Neuromab	Cat#: 73-054; RRID: AB_10671176
rabbit anti-ELKSα (LAC: A55)	Abcam	Cat#: ab50312 RRID: AB_869944
rabbit anti-ELKS2α (LAC: A136)	(Held et al., 2016)	E3-1029
rabbit anti-ELKS2αB (LAC: A143)	Abcam	Cat#: ab27250; RRID: AB_731499
rabbit anti-GFP (LAC: A146)	(Han et al., 2004), gift from Dr. T.C. Südhof	RRID: AB_2636878, T3743
rabbit anti-GFP (LAC: A211)	MBL International	Cat#: MBL_598; RRID: AB_591816
mouse anti-HA (LAC: A12)	Biolegend	Cat#: 901501; RRID: AB_2565006
rabbit anti-Liprin-α3 (LAC: A35)	(Schoch et al., 2002), gift from Dr. T.C. Südhof	RRID: AB_2617056, 4396
mouse anti-Map2 (LAC: A108)	Sigma-Aldrich	Cat#: M4403; RRID: AB_477193
rabbit anti-MAP2 (LAC: A139)	Synaptic Systems	Cat#: 188 002; RRID: AB_2138183
rabbit anti-Munc13-1 (LAC: A72)	Synaptic Systems	Cat#: 126 103; RRID: AB_887733
mouse anti-PSD-95 (LAC: A149)	UC Davis/NIH Neuromab	Cat#: 73-028; RRID: AB_10698024
rabbit anti-RIM1 (LAC: A58)	Synaptic Systems	Cat#: 140 003; RRID: AB_887774
rabbit anti-RIM1-Zn (LAC: A148)	(Kaeser et al., 2008), gift from Dr. T.C. Südhof	Q703
rabbit anti-RIM-BP2 (LAC: A126)	Synaptic Systems	Cat#: 316 103; RRID: AB_2619739
mouse anti-Synapsin-1 (LAC: A57)	Synaptic Systems	Cat#: 106 001; RRID: AB_2617071
guinea pig anti-Synaptophysin (LAC: A106)	Synaptic Systems	Cat#: 101 004; RRID: AB_1210382
rabbit anti-Synaptophysin (LAC: A64)	Synaptic Systems	Cat#: 101 002; RRID: AB_887905
goat anti-guinea pig Alexa Fluor 488 (LAC: S3)	Thermo Fisher	Cat#: A11073; RRID: AB_2534117
goat anti-rabbit Alexa Fluor 488 (LAC: S5)	Thermo Fisher	Cat#: A-11034; RRID: AB_2576217
goat anti-mouse IgG1 Alexa Fluor 488 (LAC: S7)	Thermo Fisher	Cat#: A-21121; RRID: AB_2535764
goat anti-mouse IgG1 Alexa Fluor 546 (LAC: S12)	Thermo Fisher	Cat#: A-21123; RRID: AB_2535765
goat anti-rabbit Alexa Fluor 546 (LAC: S16)	Thermo Fisher	Cat#: A-11035; RRID: AB_2534093
goat anti-mouse IgG2a Alexa Fluor 555 (LAC: S20)	Thermo Fisher	Cat#: A-21137; RRID: AB_2535776
goat anti-guinea pig Alexa Fluor 633 (LAC: S34)	Thermo Fisher	Cat#: A-21105; RRID: AB_2535757
goat anti-mouse peroxidase-conjugated (LAC: S52)	MP Biologicals	Cat#: 0855550; RRID: AB_2334540
goat anti-rabbit peroxidase-conjugated (LAC: S53)	MP Biologicals	Cat#: 0855676; RRID: AB_2334589
Chemicals, Peptides, and Recombinant Proteins		
Picrotoxin	Tocris Bioscience	Cat#: 1128
6-Cyano-7-nitroquinoxaline-2,3-dione (CNQX)	Tocris Bioscience	Cat#: 0190
D-amino-5-phosphonopentanoic acid (D-AP5)	Tocris Bioscience	Cat#: 0106

REAGENT or RESOURCE	SOURCE	IDENTIFIER
L-amino-5-phosphonopentanoic acid (L-AP5)	Tocris Bioscience	Cat#: 0107
QX314-Cl	Tocris Bioscience	Cat#: 2313
Tetrodotoxin (TTX)	Tocris Bioscience	Cat#: 1078
Experimental Models: Cell Lines		
HEK293T cells	ATCC	Cat#: CRL-3216 RRID: CVCL_0063
Experimental Models: Organisms/Strains		
Mouse: STOCK *Rims1*^{tm3Sud}/J	(Kaeser et al., 2008)	RRID: IMSR_JAX:015832
Mouse: STOCK *Rims2*$^{tm1.1Sud}$/J	(Kaeser et al., 2011)	RRID: IMSR_JAX:015833
Mouse: STOCK *Erc1*$^{tm2.1Sud}$/J	(Liu et al., 2014)	RRID: IMSR_JAX:015830
Mouse: STOCK *Erc2*$^{tm1.2Sud}$/J	(Kaeser et al., 2009)	RRID: IMSR_JAX:015831
Mouse: Cacna1a conditional knockout	(Todorov et al., 2006)	N/A
Mouse: Cacna1b conditional knockout, Cacna1b$^{tm1a(KOMP)Wtsi}$	(Held et al., 2020)	Cat# KOMP: CSD34514; RRID: IMSR_KOMP: CSD34514-1a-Wtsi
Mouse: Cacna1e conditional knockout	(Pereverzev et al., 2002)	N/A
Recombinant DNA		
pcDNA Ca_V α2δ1 (lab plasmid code (LPC): p752)	Addgene, (Lin et al., 2004)	Cat#: 26575 RRID: Addgene_26575
pCMV β4-Zn-mVenus (LPC: p910)	This paper	N/A
pCMV Cerulean-Ca_V2.1 (LPC: p773)	This paper	N/A
pcDNA Munc13-1-tdTomato (LPC: p888)	(Emperador-Melero et al., 2021)	N/A
pFSW EGFP Δcre (LPC: p010)	(Liu et al., 2014)	N/A
pFSW EGFP cre (LPC: p009)	(Liu et al., 2014)	N/A
pFUGW RIM1α-HA (LPC: p591)	(de Jong et al., 2018)	N/A
pFSW RIM1α-HA (LPC: p592)	This paper	N/A
pFSW HA-ELKS1αB (LPC: p311)	(Nyitrai et al, 2020)	N/A
pFSW HA-ELKS2αB (LPC: p314)	This paper	N/A
pFSW RIM1-Zn-HA (LPC: p654)	This paper	N/A
pFSW RIM1-PDZ-HA (LPC: p648)	This paper	N/A
pFSW RIM1-C_2B-HA (LPC: p647)	This paper	N/A
pFSW RIM1-ΔZn-HA (LPC: p640)	This paper	N/A
pFSW RIM1-ΔPDZ-HA (LPC: p639)	This paper	N/A
pFSW RIM1-ΔC_2A-HA (LPC: p637)	This paper	N/A
pFSW RIM1-ΔC_2B-HA (LPC: p638)	This paper	N/A
pFSW Ca_Vβ4-HA (LPC: p757)	This paper	N/A
pFSW β1b-Zn-HA (LPC: p659)	This paper	N/A
pFSW β3-Zn-HA (LPC: p660)	This paper	N/A
pFSW β4-Zn-HA (LPC: p661)	This paper	N/A
pFSW Zn-HA-Ca_V2.1 (LPC: p662)	This paper	N/A
pFSW HA-Ca_V2.1-Zn (LPC: p664)	This paper	N/A

REAGENT or RESOURCE	SOURCE	IDENTIFIER
pFSW Zn-HA-ELKS2αB (LPC: p657)	This paper	N/A
pFSW HA-Zn-Liprin-α3 (LPC: p658)	This paper	N/A
pFSW Zn-HA-PDZ (LPC: p656)	This paper	N/A
pFSW β4-Zn(K144/146E)-HA (LPC: p898)	This paper	N/A
pFSW Tom20-Cerulean (LPC: p049. mitoC)	(Nyitrai et al., 2020)	N/A
pFSW Tom20-Cerulean-Zn (LPC: p666, mitoC-Zn)	This paper	N/A
pFSW mito-DsRed2 (LPC: p057)	(Nyitrai et al., 2020)	N/A
Software and Algorithms		
Fiji/ImageJ	NIH	RRID: SCR_002285, https://imagej.net/software/fiji/downloads
Prism	GraphPad	RRID: SCR_002798, https://www.graphpad.com/
pClamp	Molecular Devices	RRID: SCR_011323; https://www.moleculardevices.com/products/software/pclamp.html
MATLAB	MathWorks	RRID: SCR_001622, https://www.mathworks.com/products/matlab.html